POLITECNICO DI TORINO
Repository ISTITUZIONALE

Optimization of binary binder blends for aqueous-based slurries of SiOx/C for next-generation lithium-ion batteries

Original
Optimization of binary binder blends for aqueous-based slurries of SiOx/C for next-generation lithium-ion batteries / Tamboia, L., Montinaro, G., Ravesio, E., Amici, J., Francia, C., Bodoardo, S., Bella, F., Versaci, D.. - In: JOURNAL OF CLEANER PRODUCTION. - ISSN 0959-6526. - 554:(2026), pp. 1-17. [10.1016/j.jclepro.2026.148153]

Availability:
This version is available at: 11583/3009469 since: 2026-03-31T15:48:18Z

Publisher:
Elsevier

Published
DOI:10.1016/j.jclepro.2026.148153

Terms of use:

This article is made available under terms and conditions as specified in the corresponding bibliographic description in the repository

Publisher copyright

(Article begins on next page)

30 October 2026

Journal of Cleaner Production 554 (2026) 148153

Contents lists available at ScienceDirect

Journal of Cleaner Production

journal homepage: www.elsevier.com/locate/jclepro

Optimization of binary binder blends for aqueous-based slurries of SiO_x/C for next-generation lithium-ion batteries

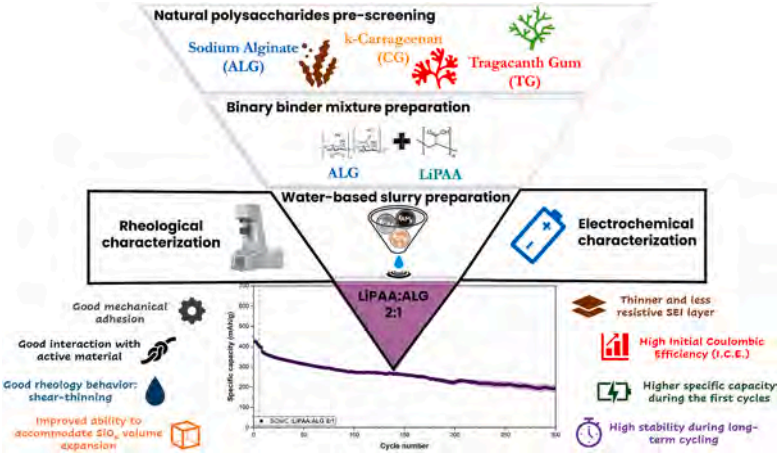
Lorenzo Tamboia, Giorgio Montinaro, Elisa Ravesio, Julia Amici, Carlotta Francia, Silvia Bodoardo, Federico Bella, Daniele Versaci *

Politecnico di Torino, Department of Applied Science and Technology, Electrochemistry Group, Corso Duca degli Abruzzi, 24, 10129, Turin, Italy

HIGHLIGHTS

- k-carrageenan excluded due to poor coating and gel-like behaviour.
- ALG and LiPAA mixture improves both cycling and manufacturability.
- 2_{LiPAA}:1_{ALG} formulation outperforms single-binder systems.
- LiPAA improves ICE while ALG ensures long-term cycling stability.
- Statistical analysis confirms LiPAA boosts initial capacity.

GRAPHICAL ABSTRACT



ARTICLE INFO

Keywords:
Lithium-ion battery
Aqueous binder
Binary binder mixture
Anode slurry
SiO_x/C active material
Energy density
Cycling stability

ABSTRACT

The growing demand for sustainable energy solutions has highlighted the crucial role of lithium-ion batteries (LIBs) in the global energy transition. However, the conventional use of polyvinylidene fluoride (PVDF) binders combined with toxic solvents like N-methyl-2-pyrrolidone (NMP), in the LIBs manufacturing process, poses environmental and cost concerns. In this study, three different water-soluble polysaccharides, sodium alginate, tragacanth gum, and carrageenan, are investigated as suitable binders for silicon/graphite composite anodes. The three single polysaccharide binders are initially screened through rheological and electrochemical analyses to ensure compatibility with slurry processing, electrode and cell manufacturing. From the pre-screening, sodium alginate emerges as the most promising candidate, demonstrating favourable rheological properties and electrochemical stability. To further improve electrode mechanical properties and long-term electrochemical performances, sodium alginate is mixed with lithiated polyacrylic acid in binary mixtures with a total binder content of 3 wt%. The optimal formulation, 2_{LiPAA}:1_{ALG}, exhibits enhanced cycling stability and higher specific capacity retention compared to single-binder systems. Statistical analysis confirms the significant influence of binder

* Corresponding author.
E-mail address: daniele.versaci@polito.it (D. Versaci).

https://doi.org/10.1016/j.jclepro.2026.148153
Received 5 August 2025; Received in revised form 15 March 2026; Accepted 27 March 2026
Available online 31 March 2026
0959-6526/© 2026 The Authors. Published by Elsevier Ltd. This is an open access article under the CC BY-NC-ND license (http://creativecommons.org/licenses/by-nc-nd/4.0/).

mixture composition, highlighting the complementary mechanical and electrochemical roles of ALG and LiPAA. In comparison with previously reported crosslinked or grafted binder systems that require chemical modification, this approach uses a simple physical mixing strategy, improving the electrochemical behaviour, preserving processability. Overall, the results demonstrate that rationally designed combinations of natural and synthetic water-soluble binders offer a viable strategy to balance mechanical integrity, sustainability, and electrochemical performance, providing valuable insights for the development of next-generation LIB anodes.

1. Introduction

Introduced into the market in 1991, lithium-ion batteries (LIBs) have experienced continuous and steady growth. Their development has been closely tied to the rapid technological advancements of recent decades, making them the most widely used energy storage systems for a broad spectrum of devices. At the same time, the constant advancement in battery performances has driven technological innovation, as well as the proliferation of new electronic devices, both small and large, which have become an integral part of our daily lives (Li et al., 2018).

Today, LIBs are used not only in smartphones and laptops, but also in advanced medical machinery, tools, drones, bicycles, electric vehicles, and energy storage devices for renewable energy sources. Thanks to their increasingly advanced performance, such as high energy density, long lifespan, and fast charging capabilities, these batteries can play a crucial role in the transition to a more sustainable energy system. For example, LIBs can support the large-scale adoption of renewable energy sources and significantly contribute to the decarbonization of the transportation sector, steering toward a future with reduced carbon emissions (Golombek et al., 2022; Mehigan et al., 2022; Kim et al., 2023).

However, some key aspects still need to be improved. They primarily concern the materials used in battery production, but also the overall manufacturing process and the ability to effectively recycle materials at the end of the battery lifecycle. In the past years, the major efforts to enhance the LIBs performances have predominantly focused on studying and developing the active materials directly involved in the electrochemical processes (Rolandi et al., 2024). More recently, greater attention has been paid to the entire manufacturing process of batteries, emphasizing not only performance, but also cost efficiency and sustainability of the overall production chain (Dühnen et al., 2020). This shift has driven the research community to also focus its attention on other essential battery components, which are fundamental but not directly involved in the electrochemical reactions, commonly referred to as “inactive electrode materials” (Streipert et al., 2020). Among them, even if present in small quantities (2-5 % by weight), the polymeric binder plays a crucial role in the proper functioning of the batteries, ensuring the structural integrity of the electrode by holding its components together, and providing strong adhesion to the current collector, consequently allowing efficient electrochemical reactions (Rolandi et al., 2024; Yang et al., 2024).

During the last years, the exploration of new binders quickly shifted to water-soluble materials, primarily due to their greater eco-sustainability. Notably, N-methyl-2-pyrrolidone (NMP), commonly used to dissolve polyvinylidene fluoride (PVDF), is reprotoxic and teratogenic, contributing to health hazards and environmental pollution during production and disposal processes. Additionally, eliminating toxic and costly solvents, like NMP, from the manufacturing process offers significant economic benefits: using water-soluble binders is significantly cheaper than PVDF and enables 40 % energy savings in electrode manufacturing, compared to an organic solvent-based process (Bresser et al., 2018; Liu et al.). Beyond these advantages, the use of water-soluble binders supports the important concept of “design for recycling”. In fact, numerous studies have demonstrated that aqueous binders enable quicker, more efficient, and cost-effective separation of electrode components during the recycling process, simplifying the battery end-of-life disposal (Rolandi et al., 2024; Scott et al., 2023). At the same time, some recent studies have focused on the development of alternative, completely fluorine-free binders for the fabrication of next-generation LFP and NMC-based cathodes (Zhang et al., 2021; Montes et al., 2024; Leibetseder et al., 2024).

Finally, the increasing interest in silicon-based anode electrodes, able to enhance the electrochemical performance of batteries, has made the use of aqueous binders essential. In fact, silicon, despite its huge specific capacity (4200 mAh/g for $Li_{4.4}Si$), is characterized by one significant drawback: it undergoes a volume expansion of over 300 % during the lithiation process. This huge expansion causes mechanical issues in the electrode structure, leading to dramatic capacity fading (Yang et al., 2024; Li et al., 2021a). In this frame, the binder, although present in small quantities, can play a fundamental role, as demonstrated in some recent studies. As an example, Vanpeene et al. investigated the addition of cations to CMC binder able to improve the performance of silicon-based anodes. In particular, they investigated how Zn^{2+} coordinates with the CMC carboxylate groups, forming a cross-linked network that enhances the electrode mechanical properties. Using the combination of *in operando* and in situ X-ray tomography, the authors show that the coordinated binder reduces cracking, limiting irreversible expansion, and maintaining better adhesion to the current collector during cycling. In addition, they observed that the coordinated binder leads to a more uniform SEI layer, decreasing the electrolyte degradation upon cycling (Vanpeene et al., 2025).

Sedlatschek et al. used in operando SEM to study graphite–SiO_x based electrode during cycling. They observed that SiO_x particles did not crack during the initial cycles, but the electrode exhibited significant particle rearrangement and local strain, mainly due to binder cracking. This means a progressive loss of adhesion, which leads to structural rearrangements, increased internal resistance, and gradual capacity fade. These results highlight that mechanical degradation of the binder network, rather than fracture of the active material particles, is the initial factor of driving capacity fade and performance loss (Sedlatschek et al., 2025). More generally, as widely reported, binders rich in functional groups such as hydroxyl (-OH), carboxyl (-COOH), amino (-NH_2), amide (-$CONH_2$), etc., can effectively mitigate the mechanical stresses caused by the volumetric expansion of silicon particles. This is possible thanks to the formation of hydrogen bonds between the functional groups of the binders and SiO_x on the surface of silicon particles, which preserves the structural integrity throughout the electrochemical process (Yang et al., 2024). Among aqueous binders, the polysaccharide sodium carboxymethylcellulose deserves a special mention. Since the preliminary studies by Drofenik et al. (2003), it has emerged, combined with styrene-butadiene rubber (SBR), as the main choice for the production of graphite-based anodes and lithium iron phosphate-based cathodes. Subsequently, a variety of other natural polysaccharides have been investigated, primarily for silicon-based anodes, thanks to their richness in hydroxyl and carboxyl functional groups. These include sodium alginate, guar gum, xanthan gum, chitosan, and many others (Bresser et al., 2018). At the same time, synthetic binders such as polyacrylic acid (PAA) have garnered significant attention, thanks to the strong interactions with silicon particles, the high elasticity, and the capability to mitigate Si volume expansion (Yang et al., 2024; Li et al., 2021a). However, common polysaccharides suffer from poor tensile properties, resulting in insufficient electrode structure stabilisation during the lithiation/de-lithiation process. Similarly, PAA tends to consume lithium ions during the solid electrolyte interphase (SEI)

formation process, resulting in low initial Coulombic efficiency (ICE) and a subsequent capacity decay in Si-based anodes. Meanwhile, the lithiated PAA (Li-PAA) has shown limited volume changes mitigation during cycling. Overall, all these binders possess a one-dimensional structure that cannot completely suppress the volume expansion of silicon particles. As a result, significant attention has been paid toward developing 3D structures, often by combining two or more binders through grafting, crosslinking, or similar processes (Yang et al., 2024; Li et al., 2021a). Recent studies show that the formation of crosslinked polymer networks, obtained by linking different polymers through covalent bonds, ionic interactions, or hybrid structures, can potentially increase the mechanical strength, adhesion of the active material, and stabilize the SEI layer, allowing for improved electrical contact and better electrode cyclability (Zhong et al., 2024; Yi et al., 2025; Lai et al., 2022). For instance, PAA has frequently been combined with polysaccharides such as chitosan, sodium alginate, and CMC (Song et al., 2019; Zhao et al., 2018; Hu et al., 2021). However, the use of crosslinked systems still presents some critical issues related to the high stiffness of the networks, the complexity of the synthetic processes, the difficulty of processability of the slurries, and the resulting additional costs, which limit their feasibility and scalability for industrial or pre-industrial applications (Zhong et al., 2024; Yi et al., 2025; Lai et al., 2022).

This study presents an in-depth screening of several natural binders to assess their suitability for anodic formulations based on commercial silicon suboxides/carbon combination (SiO_x/C). The selected binders are bio-derived materials with high natural availability, including sodium alginate (Guo et al., 2019), tragacanth gum (Versaci et al., 2023) and carrageenan (Cuesta et al., 2015; Li et al., 2021b; Jang et al., 2022), all of which are rich in carboxylic and hydroxyl groups. Among these, the most promising binder was further investigated in a binary mixture with LiPAA in different proportions. The evaluation of the binary binder mixture was performed using simple linear regression and analysis of variance (ANOVA) to study the effects of binder percentage on specific performance responses. This methodological approach also facilitated the investigation of potential correlations between the binder ratio and the observed outcomes, providing a comprehensive understanding of its influence on the system behaviour (Román-Ramírez and Marco, 2022). Simultaneously, considerable attention was focused on the study of the rheological behaviour of the binder mixtures and corresponding slurries. This analysis offered valuable insights into the processability and scalability of the system, ensuring that the optimal binder formulation among the investigated ones guarantees the best overall performance and manufacturability of the electrodes.

2. Material and methods

The following section introduces the experimental methodology and the techniques used for material and cell characterization.

2.1. Anode manufacturing and electrochemical characterization

The binders evaluated included sodium carboxymethyl cellulose (CMC, Mw: 1700 kDa, DS: 0.8 - 1.0, Daicel CMC2200, Aboshi, Japan), sodium alginate derived from brown algae (ALG, Mw: 200 kDa, Sigma-Aldrich, St. Louis, MO, USA), tragacanth gum (TG, Mw: 600 – 800 kDa, Sigma-Aldrich, St. Louis, MO, USA), carrageenan (CG, Mw: 300 – 500 kDa, Sigma-Aldrich, St. Louis, MO, USA) and polyacrylic acid (PAA, 250 kDa, 35 wt %, Sigma-Aldrich, St. Louis, MO, USA). The PAA was lithiated using lithium hydroxide monohydrate ($LiOH{\cdot}H_2O$) at a molar ratio of 1:1 (PAA:$LiOH{\cdot}H_2O$) in an aqueous solution. Successively, the binary binder mixtures were prepared with weight ratios of 1_{LiPAA}:2_{ALG}, 1_{LiPAA}:1_{ALG}, and 2_{LiPAA}:1_{ALG}. All solutions were prepared at a concentration of 4 wt.% using deionized ultrapure Milli-Q water to ensure complete binder solubilization. pH measurements were performed using a pH meter (pH 60 DHS, XS Instruments). All measurements were conducted at a controlled temperature of 25 °C to minimize the impact of temperature fluctuations on the results.

For the slurry preparation, a commercial partially oxidized SiO_x/C composite (D50: 16 ± 2 μm, tap density: 1.15 ± 0.05 g/cm^3, specific surface area: 1 ± 0.5 m^2/g, MTI® Corp., Richmond, CA, USA) was selected as the active material, constituting 95 wt % of the total solid mass. Carbon black C-NERGY™ Super C45 (BET surface area: 45 m^2/g, Imerys, Paris, France) was added at 2 wt % as the conductive additive, while the binder constituted the remaining 3 wt %.

The mixing protocol initially involved the combination of the entire amount of solvent with the binder using a mechanical impeller overhead mixer (ARGOlab AM20-D, ARGOlab, Modena, Italy) at 1000 rpm. Successively, the conductive additive (carbon black) was added, followed by the active material (SiO_x/C) addition. The mixing process continued for a total of 3 h to ensure a homogeneous particle dispersion. The resulting slurry was cast onto the copper current collector using an automatic film applicator (AB4120 TGC Sheen®) and a doctor blade set to a fixed thickness of 100 μm, at an application speed of 10 mm/s and dried in an oven at 50 °C for 1 h in an air atmosphere. Subsequently, electrodes with areas of 1.77 cm^2 and 0.79 cm^2 were cut out for galvanostatic cycling and cyclic voltammetry test, respectively, vacuum dried at 120 °C for 4 h (Büchi Glass Oven B-585), and transferred into an Ar-filled glovebox (MBraun Labstar, H_2O and O_2 content <1 ppm) for the assembly of two- (Coin cell 2032) and three-electrode (Swagelok-type) cells. The final mass loading of the electrodes ranged from 3.2 to 4.2 mg/cm^2 and it was verified by sampling performed on 15 electrodes for each coating obtained. For all the electrochemical tests, glass fiber separator (Whatman) was filled with an electrolyte consisting of 1M $LiPF_6$ 1 M dissolved in a 1:1 mixture of ethylene carbonate (EC) and diethyl carbonate (DEC), with 10 % of fluoroethylene carbonate (FEC) and 2 % of vinylene carbonate (VC) (Solvionic, Toulose, France).

For the electrochemical stability test, the binder solutions were casted upon the collectors using the same parameters previously applied for the slurry. The electrochemical reactivity of the binders was evaluated by testing the resulting electrodes (0.79 cm^2) in a three-electrode cell (T-cell) with lithium metal disks used as both the reference and counter electrodes. The voltage range was set between 0.01 and 2 V with a scan rate of 0.1 mV/s and the measurements were conducted using a versatile multichannel potentiostat (VMP-3 Biologic, Grenoble, France). The same voltammetry test was carried out on half-cell containing SiO_x/C electrodes manufactured with different binder formulations.

The electrochemical characterization including galvanostatic charge/discharge cycling was carried out using an ARBIN LBT-210 battery tester at room temperature. The test was conducted in half-cell configuration, using lithium metal as the counter electrode, in a voltage range of 0.01 to 1.5 V. The cycling protocol included a constant current discharge step up to 0.01 V followed by a constant voltage step (CV) fixed at 0.01 V, maintained until a specific current was reached, to ensure complete lithiation of the silicon oxide particles, finishing with a constant current charge step up to 1.5 V. Specifically, the rate capability cycling protocol starts with an initial 5-cycle loop to allow a stable SEI layer formation. Each cycle consisted of a constant current (CC) discharge at C/10, followed by a constant voltage (CV) hold at 0.01 V until the current decreased to C/100, and concluded with a CC charge at C/10. This was followed by sequential cycling steps: 5 cycles at CC C/5 with CV C/50, 5 cycles at CC C/2 with CV C/20, 5 cycles at CC 1C with CV C/10, 5 cycles at CC 2C with CV C/5, and, finally, 5 cycles at CC 1C with CV C/10, with a total test duration of 30 cycles. The long cycling protocol adopted consisted of 3 cycles at CC C/10 and CV C/100, followed by 5 cycles at CC C/5 and CV C/50, and then 292 cycles at 1C and CV C/10, totalling 300 cycles. Potentiostatic electrochemical impedance spectroscopy (PEIS) analyses were conducted on a versatile multichannel potentiostat (VMP-3 Biologic). Alternative current (AC) impedance measurements were performed before cycling with an amplitude of 10 mV over a frequency range of 100 kHz–100 MHz, after three formation cycles at C/10 and after the rate capability (RC) test.

2.2. Rheological characterization

The rheology tests were performed on solutions containing 2.4 wt % binder, maintaining the same binder-to-water ratio as in the slurry formulation, using a rotational rheometer (NETZSCH Kinexus Prime pro+, Selb, Germany). Rheology tests were also performed on the slurry using the aforementioned instrument to monitor the viscosity of the slurry at various shear rates. The tests were conducted over a 10^{-2} to 10^{3} 1/s shear rate range, using a cone-plate geometry with a 4° angle and a 40 mm diameter. Additionally, the elastic and viscous moduli of both the binder solutions and slurries were measured across different frequency ranges: from 10^{2} to 10^{-1} Hz for the binder solutions and from 150 to 10^{-2} Hz for the slurries, using a parallel plate geometry with a fixed gap of 0.5 mm. These measurements were performed within the linear viscoelastic region using amplitude and frequency sweep tests.

2.3. Physico-chemical characterization

Thermogravimetric analysis (TGA) was performed using a Linseis TGA PT 1600 instrument with a heating rate of 10 °C/min in air, from room temperature to 1000 °C.

Field emission scanning electron microscopy (FESEM) analysis was performed using a Zeiss SUPRA TM 40 with Gemini column and a Schottky field emission tip (tungsten at 1800 K). Images were acquired at an acceleration voltage of 3 kV, with a working distance ranging from 2.1 to 8.5 mm, and a maximum magnification of 250 kX. Energy dispersive X-rays (EDX) analysis was performed using an Oxford X-Act EDX Spectrometer (Oxford Instruments).

Self-standing pure and binder mixtures, obtained by solvent casting process and successively vacuum dried, were investigated via FT-IR spectroscopy employing a ThermoFischer Scientific FT-IR Spectrometer in a wavenumber range between 525 and 2200 cm^{-1} with 32 scans and a resolution of 4 cm^{-1} in ambient air.

2.4. Statistical analysis (simple linear regression and ANOVA)

The binary binder mixtures weight ratios were selected to achieve equidistant points in the data space. The input parameters included the weight fractions of LiPAA and ALG. A mathematical model was developed using the parameters to capture interactions and accurately predict outcomes, including the specific capacities at the 5th, 10th, 15th, 20th, 25th, and 50th cycles. Following a one factor at a time approach, the percentage of LiPAA was systematically varied while maintaining ALG as its complement to evaluate the resulting responses.

3. Results and discussion

The initial phase of this study focused on the investigation of various polysaccharides as potential binders for aqueous-based slurries. Three different binders were chosen: ALG, CG, and TG. These polysaccharides were selected as their chemical structure are rich in -COOH and -OH functional groups, and because they are widely available and eco-friendly (Dühnen et al., 2020; Bresser et al., 2018; Zhang et al., 2024). Aqueous solutions at 4 wt % of each binder were prepared to evaluate the pH, which is one of the key parameters to take into account in the slurries preparation processes. As it can be observed in Table S1, the measured pH values for the binder solutions ranged from 5.5 to 7.5, which is generally considered suitable for slurry processability. More specifically, among the binders investigated, TG exhibited the most acidic pH (5.49), whereas ALG showed the most basic pH value (7.44). It is worth noting that, as reported in the literature (Schwarz et al.), TG demonstrates its highest stability and optimal rheological properties at a slightly acidic pH (just above 5). Moreover, mildly acidic suspensions are typically preferred to achieve better electrochemical behaviour in the context of silicon-based anodes. In contrast, a highly basic pH can lead to several issues, including silicon dissolution, instability of the SEI layer and binder degradation (Dang et al., 2020). In parallel with the polysaccharide binders, LiPAA binder was investigated. The neutralisation was achieved by mixing PAA with lithium hydroxide monohydrate ($LiOH{\cdot}H_2O$). This reaction led to the formation of lithium salts, as the lithium ions reacted with the carboxyl groups in the polymer, stabilising its structure, reducing its acidity, and possibly increasing the availability of lithium in the final cell. For this study, PAA with a molecular weight of 250 kDa was selected, as previous research has demonstrated superior electrochemical performances for this specific molecular weight (Armstrong et al.; Truong et al., 2021).

Each binder solution was subsequently diluted with water to obtain a final binder concentration of 2.4 wt %, consistent with the binder to water ratio used in the final slurry formulation and was then subjected to rheological analysis. The rheological measurements included the viscosity behaviour over a range of shear rates (Fig. 1a) and the frequency sweep tests within the linear viscoelastic region of the solutions (Fig. 1b–e). The purpose was to confirm the non-Newtonian viscoelastic behaviour and shear thinning properties of the samples, and to verify that the binder solutions did not exhibit purely gel-like characteristics. In fact, pure gel-like properties can result in slurries with poor adhesion to the collector, compromising the structural integrity of the electrodes and, ultimately, reducing the electrochemical performance of the Li-ion cell (He et al., 2022; Lee et al., 2010; Reynolds et al., 2022a, 2022b). The viscosity curves (Fig. 1a) show that CMC, used as a reference in this study, exhibits significantly higher values at low shear rates compared to the other binders. This reflects a better behaviour of the solution in the resting storage regime, where a stronger network structure enhances stability and prevents particle sedimentation (Ouyang et al., 2020). Within the coating shear rate range (10–500 1/s) (Sullivan and Bose, 2022; Nguyen et al., 2015), ALG reaches viscosity levels comparable to those of CMC, while TG exhibits a constant slope, with viscosity values higher than ALG at low shear rates, which contributes to improved slurry stability. However, at higher shear rates, TG viscosity decreases, likely due to the scission of polymer chains; this behaviour is attributed to the specific composition of TG, which includes a mixture of soluble tragacanthin and gel-forming bassorin, some of which may be more susceptible to shear-induced degradation. In contrast, CG exhibits a sharp initial drop in viscosity, indicating premature mechanical degradation. In Fig. 1b–e, the elastic (G′) and storage moduli (G″), along with the phase angle, obtained as a result of the frequency sweep tests, are shown for ALG, TG, CG, and CMC, respectively, enabling a direct comparison of their viscoelastic properties. ALG, TG, and CMC exhibit liquid-like behaviour at low shear rates, as indicated by a higher phase angle. For TG and CMC, a crossover between G′ and G″ occurs at approximately 2 and 3 Hz, respectively. This crossover corresponds to the relaxation time of the binder solution. Beyond this point, the timescale becomes shorter than the relaxation time of the polymer chains, preventing them from reorganising efficiently. As a result, the binder exhibits a more elastic, solid-like behaviour, reflected by a phase angle dropping below 45° at higher frequencies (He et al., 2022). In contrast, CG exhibits gel-like properties over the entire spectrum of the analysis: G′ and G″ remain largely frequency-independent, with a low phase angle, indicating a pure solid-like response. G' > G″ confirms that the elastic component of the material response, which stores and recovers energy, outweighs the viscous component, which dissipates energy (Lee et al., 2010). When incorporated into the slurry, this pronounced gel-like behaviour resulted in poor adhesion to the collector, leading to an unfeasible coating process.

Following the initial screening, the selected polysaccharide binders were incorporated into the slurry formulation along with carbon black and the active material, of which SiO_x accounts for 6% of the total active material content, as determined by TGA (Fig. S1c). All information regarding the active material is shown in Fig. S1a–e. The 4 wt % single binder solutions were used to prepare the slurries, after which the remaining water was added to achieve a solid fraction of 45 %, ensuring better component mixing. The pH value was not significantly influenced

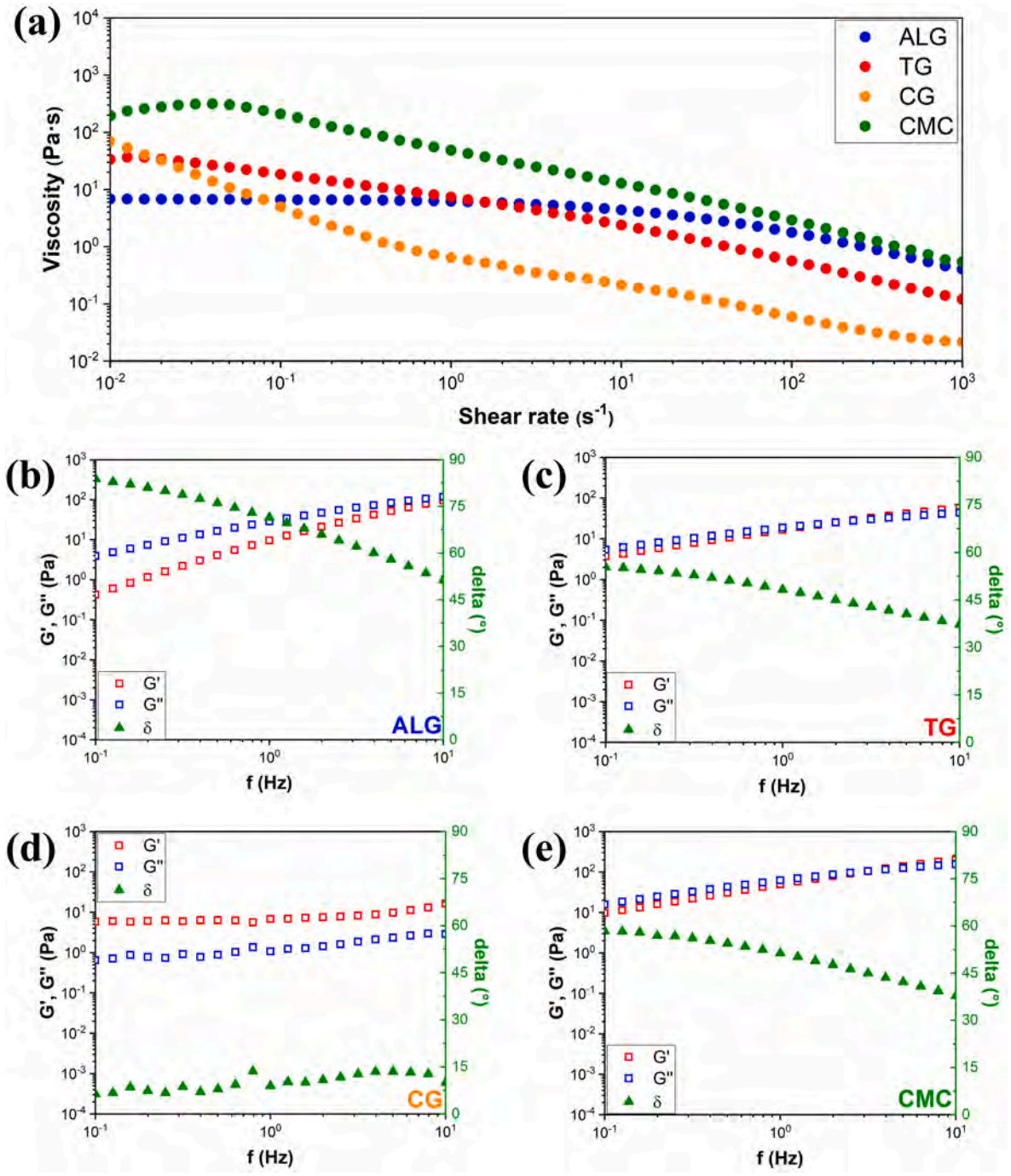


Fig. 1. Viscosity profiles of all binder solutions as a function of shear rate (a), and frequency sweep test results for ALG (b), TG (c), CG (d), and CMC (e) solutions (2.4 wt %).

by the dilution, as the binder percentage in the slurry has minimal impact on the pH. The slurry was mixed using a helical overhead stirrer for 3 h at a constant speed of 1000 rpm. This speed was consistently used for all binders, as higher speeds (*e.g.*, 2200 rpm) resulted in partial binder degradation. After the slurry mixing process, rheological tests were performed (Fig. 2). In general, all slurries exhibited increased viscosity at low shear rates compared to the corresponding pure binder solutions (Fig. 2a). This behaviour is attributed to the presence of solid particles, which make the samples more solid. However, a shear-thinning behaviour was maintained for all the slurries, highlighting the importance of the binder properties and its contribution in determining the overall slurry viscosity (Reynolds et al., 2022b). It is widely recognised that higher viscosity at low shear rates is preferable to maintain slurry homogeneity and prevent particle sedimentation, while lower viscosity at high shear rates is preferable to ensure effective coating processability (Sullivan and Bose, 2022; Nguyen et al., 2015). In the present study, the slurry containing ALG and CG exhibited higher viscosity at low shear rates, preventing sedimentation and exceeding the viscosity of the slurry prepared with CMC, despite the pure CMC solution itself being more viscous. This behaviour, indicative of the more solid-like nature of ALG and the gel-like characteristics of CG at low shear rates, was further confirmed through frequency sweep tests (Fig. S2) performed after determining the linear viscoelastic region via amplitude sweep tests. However, it is important to underline that, while

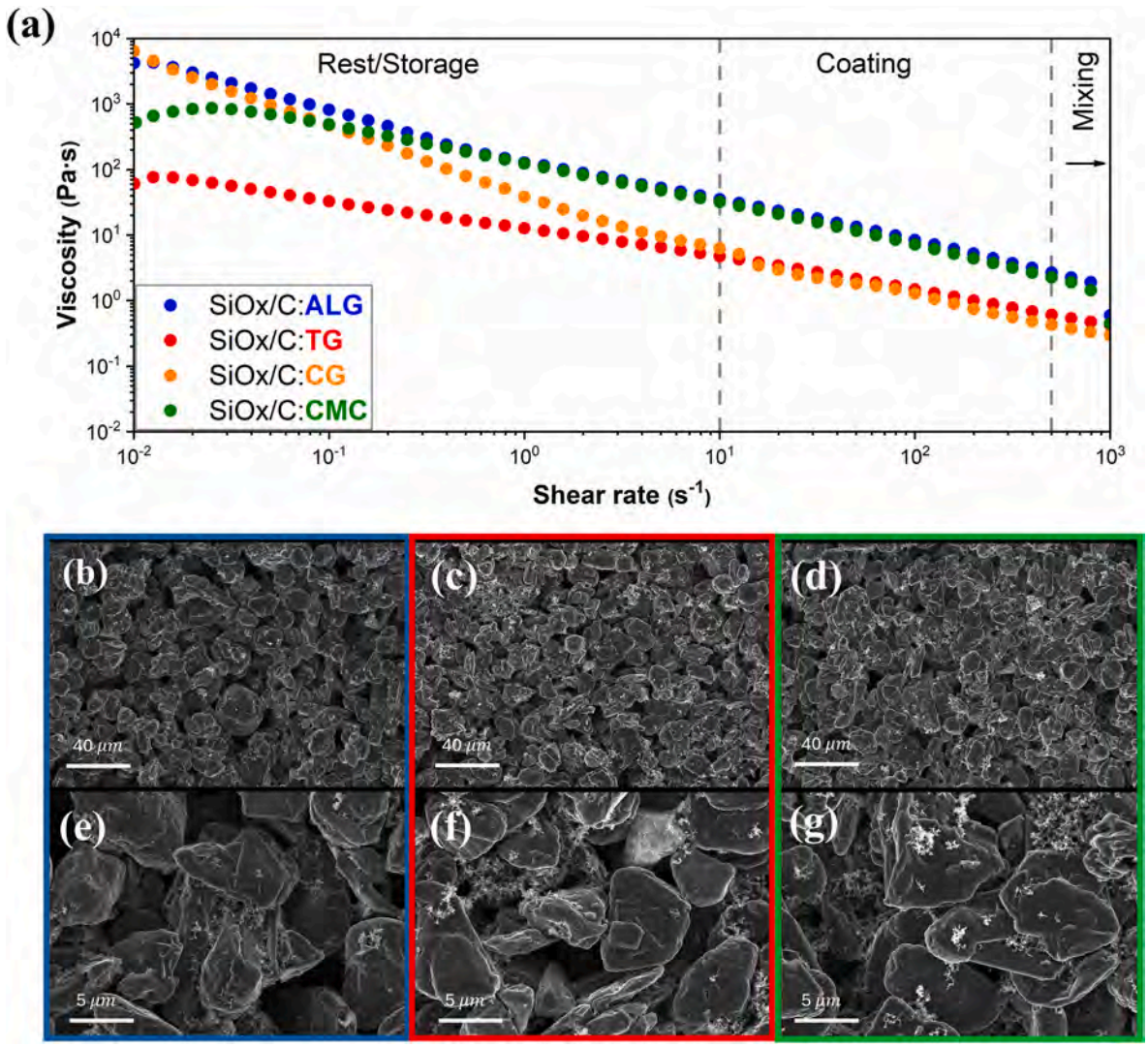


Fig. 2. Viscosity profiles of all slurries as a function of shear rate for SiO_x/C: ALG, TG, CG, and CMC (a). FESEM micrographs of pristine anode electrodes at different magnifications: 2k (a–c) and 10k (d–f), showing electrodes composed of SiO_x/C, carbon black, and various binders: ALG (b, e), TG (c, f), and CMC (d, g).

high viscosity is desirable, it should ideally be solid-like (Lim et al., 2015). Analysing G′ and G″, ALG is solid-like with G' > G″, while CG maintains a gel-like structure (G' > G″ and both moduli exhibit frequency-independent values across the entire range, Fig. S2c) (Lee et al., 2010; Kasinathan et al., 2018; Makino et al., 2024). Conversely, the slurry containing TG showed lower low-shear rate viscosity, potentially leading to increased sedimentation and phase separation. At higher shear rates, the viscosity of the slurries containing ALG and CMC became very similar, with a preferred shear-thinning behaviour that reduces the stress applied on the film applicator. This behaviour also leads to a greater G″, which facilitates uniform flow and improves the smoothness and processability of the slurry. In contrast, at higher shear rates, the observed drop in viscosity in TG and CG slurries is likely due to the breaking of polymer chains, as previously reported for binder solutions. As already mentioned, the slurry containing ALG exhibits a complete change in rheological properties when incorporated into the slurry, as opposed to when it is in the pure binder solution. This interesting behaviour suggests that the strong interaction between ALG and solid particles probably leads to a more solid and organised structure. By contrast, slurries formulated with CMC and TG retain rheological behaviour nearly identical to their respective binder solutions, making their viscosity more binder-dependent (Fig. S2b and d). According to the rheological results, and given the impossibility of obtaining a homogeneous coating, CG was excluded from the subsequent analyses.

After the slurry mixing process, the slurries were coated onto the copper current collectors and subjected to a double drying process to evaporate all the water content. Subsequently, morphological analysis was conducted on the electrodes using FESEM to further evaluate the impact of each binder on the structural integrity of the electrode. As it can be observed in Fig. 2b–g, all the electrodes show a uniform particle distribution with no signs of delamination or cracks. Even though the binders are not directly distinguishable in the FESEM micrographs due to their polymeric nature and low concentration, their presence significantly contributes to the overall uniformity of the electrode structure (Versaci et al., 2023; Tang et al., 2023; Chou et al., 2015). Indeed, the micrographs reported in Fig. 2b–g predominantly reveal larger graphite particles, characterized by their typical layered morphology, surrounded by smaller carbon black particles.

Before the electrochemical characterization of the electrode, the electrochemical stability of the binders, suitable for the electrode manufacturing, was assessed (Fig. S3a). This analysis was carried out to exclude any potential binder-electrolyte interactions or undesired electrochemical reactions within the operating potential window. In this regard, electrodes with a 10 mm diameter were prepared by depositing the pure binder solution on the copper current collector to assemble three-electrode cells for cyclic voltammetry (CV) analysis. As evidenced

in the CV profiles reported in Fig. S3a, no evident redox processes are observable, indicating that there are no undesired reactions directly attributable to the binders. This makes all investigated binders potentially implementable in SiO_x/C-based anode electrodes.

Similarly, CV analysis was performed on the SiO_x/C electrodes to assess their electrochemical behaviour within the operational voltage range (Fig. 3a and b, Fig. S3b–d). In particular, Fig. 3 compares the electrochemical behaviour of electrodes containing the three different binders at cycles 1 and 5, respectively. Observing the profiles, distinct current peaks associated with the lithiation and de-lithiation processes of the SiO_x/C active material can be clearly observed. During the first cycle, the peak intensities and their shifts vary significantly depending on the binder used. Concerning the lithiation process, two pronounced cathodic peaks are observed at approximately 0.17 V and 0.02 V. The first peak is primarily associated with the formation of amorphous Li_xSi phases, while the second corresponds to the transition from amorphous Li_xSi to crystalline $Li_{15}Si_4$ and the concomitant lithiation of graphite to LiC_6 (Legerstee et al., 2022; Liu et al., 2023; Yin et al., 2018; Mukanova et al., 2018). This behaviour is particularly evident in the electrode containing ALG, where the well-defined redox peaks shift toward higher potentials indicates reduced cell polarization. This lower system polarization suggests a more efficient utilization of the active material. In contrast, higher resistivities are observable in SiO_x/C:TG and SiO_x/C:CMC electrodes, evidenced by a less defined peak at 0.17 V for the TG-based electrode and the complete absence of this peak in the CMC-based electrode. Additionally, both electrodes exhibit less pronounced peaks at lower potentials, near the cut-off voltage of 0.02 V. Regarding the first anodic scan of the SiO_x/C:ALG electrode, distinct and intense peaks are observed, with a shoulder appearing at approximately 0.15 V and two overlapping peaks appearing between 0.23 and 0.27 V. These observations further confirm the lower internal resistance of the cell, as previously evidenced in the initial cathodic scan. The shoulder and the first overlapping peak correspond to the de-lithiation of graphite, while the second peak is attributed to the de-alloying of silicon, corresponding to the initial phase transition from a-Li_xSi to the a-Si phase (Yan et al., 2023; Ravesio et al., 2025). In contrast, electrodes fabricated with TG and CMC both exhibit a broader peak between 0.23 V and 0.27 V, indicative of their higher internal resistance. A third peak is observed for all electrodes at higher potentials, around 0.5 V, suggesting an additional silicon dealloying step (Xu et al., 2010). For the fifth cycle (Fig. 3b), the peak profiles become more similar for all three binders. In fact, the cathodic scan at the fifth cycle indicates improved alloying/intercalation of lithium ions into the active material, as evidenced by the consistent position and definition of anodic peaks for all electrodes. Analogously, increasing the number of cycles, the anodic peak at 0.5 V significantly weakens, while the broad peak at 0.22 V – 0.27 V becomes more pronounced for TG- and CMC-based electrodes. This suggests a more facile oxidation process, which is closely linked to the reversible reaction occurring at the a-Si domains (Zhang et al., 2014; Sun et al., 2016; Abel et al., 2012). In conclusion, the current intensities of both cathodic and anodic peaks increased with the number of cycles, attributed to the activation of the active material and the enhancement of Li-ion conductivity in the electrode (Ravesio et al., 2025). However, the lower polarization observed for electrodes using sodium alginate as a binder supports the idea that its stronger interaction with the active material enhances the electrochemical performance of the cell. This may also result from its ability to better accommodate volume expansion, contributing to improved electrode stability during cycling. CMC and TG, on the other hand, appear to share a similar structure, which could explain their comparable ionic transport and gradual activation.

Starting from the results obtained from cyclic voltammetry, all electrodes with different binders were subjected to repeated charge/discharge cycles at different C-rates. This protocol aims to evaluate the rate capability by applying increasing currents to the cells, simulating the more demanding conditions that may arise during battery operation. Fig. 4a–i, presents the average specific charge capacity of electrode incorporating the three selected binders: ALG, TG, and CMC. Each electrode composition, distinguished by binder, was characterised using five coin cell replicas. Table S3 summarises the average mass loading of the electrodes containing different binders.

As expected, the electrodes containing CMC as a binder exhibited high capacity up to 1C, demonstrating huge capacity recovery after cycling at 2C. However, electrodes with ALG exhibited better electrochemical behaviour compared to those with TG throughout all investigated cycles, particularly achieving a higher average specific capacity. Interestingly, at higher C-rate (*e.g.,* 2C), the electrodes with ALG and TG exhibited less capacity variability and better capacity retention compared to the cells assembled with CMC-based electrodes. This can be attributed to the higher presence of carboxyl groups and hydrogen bonds, which interact more effectively with the oxidized Si surface compared to CMC (Kovalenko et al., 1979; Yuca et al., 2022). This is in agreement with what was observed in previous rheological and cyclic voltammetry analyses, which suggest a better interaction between the SiO_x/C particles and the sodium alginate, and which translates into better performances, especially at high C-rates.

To better assess the electrochemical processes occurring for each

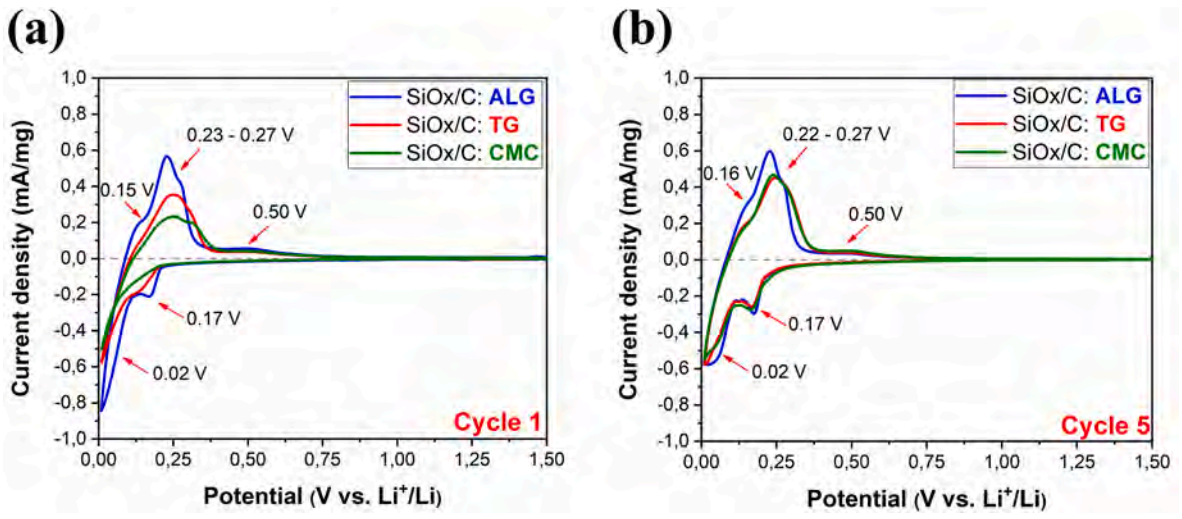


Fig. 3. Cyclic voltammetry at a scan rate of 0.1 mV/s of electrodes with all components (binder, active material, and conductive material) at cycle 1 (a) and cycle 5 (b).

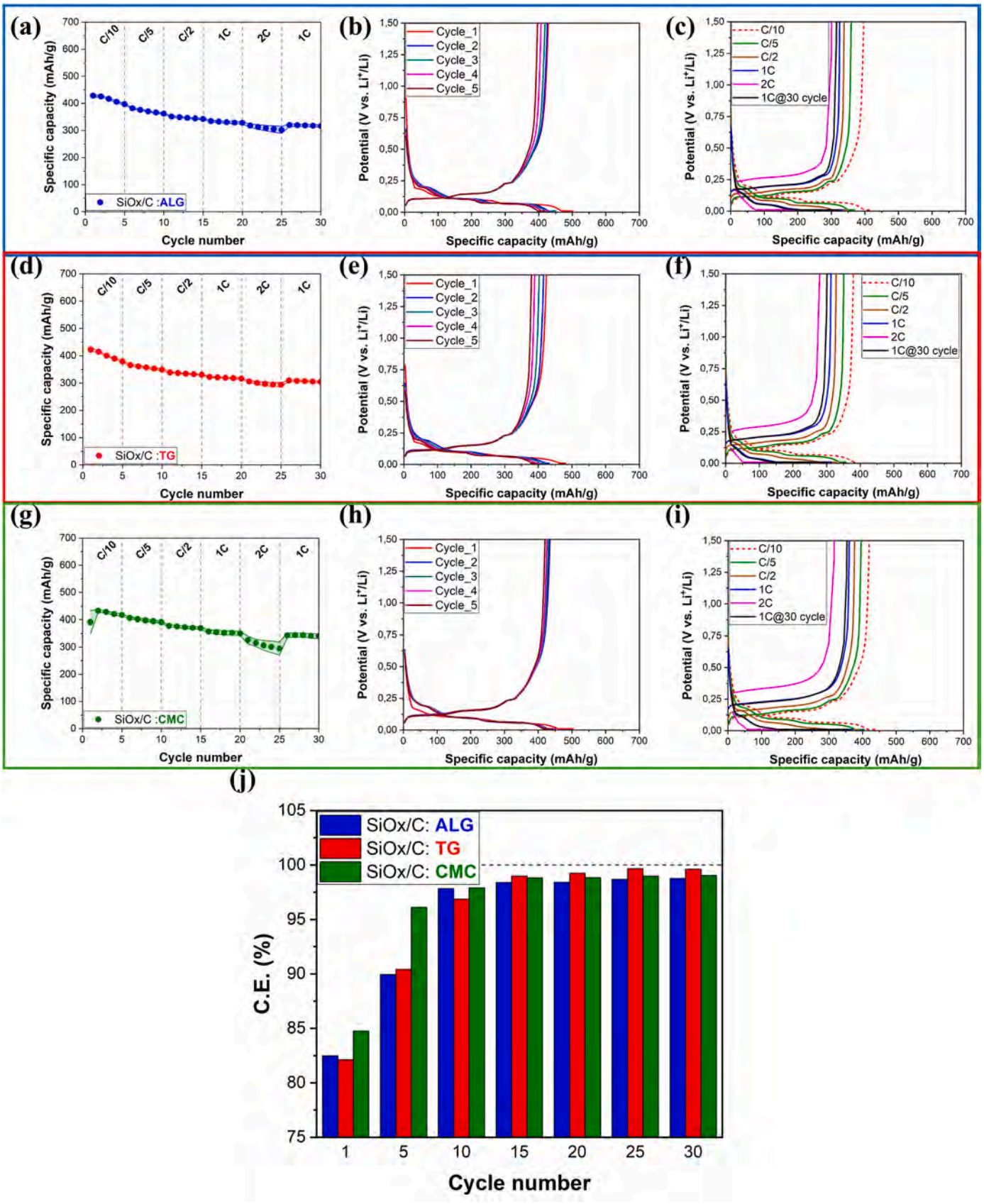


Fig. 4. Average specific capacity of electrodes with selected binders, measured up to 30 cycles, charge and discharge profiles during the forming cycles and at different C-rates, for the most representative electrodes containing ALG (a-c), TG (d-f), and CMC (g-i). Average CE of the electrodes with selected binders, measured up to 30 cycles.

different formulation, the charge/discharge profiles of the most representative cells, assembled using electrodes with the three selected binders, are reported in Fig. 4b–e,h. Focusing on the first forming cycle, during the first lithiation process of the SiO_x/C composite, a voltage plateau around 0.2 V is observable, which is slightly lower than the subsequent cycles. This behaviour is likely due to increased internal resistance associated with lower electrolyte permeation during the initial cycle and the first lithiation of SiO_x. However, all the subsequent charge/discharge profiles show the typical multistage process characteristic of the graphite lithiation overlapped with the silicon lithiation process. In fact, graphite is typically active below 0.25 V vs. Li^+/Li, while silicon operates within 0.05 – 0.6 V (Magasinski et al., 2010; Chen et al., 2022; Obrovac and Christensen, 2004). During the graphite staging mechanism, lithium preferentially occupies specific sites within the graphite layers; once these sites are fully occupied, lithium insertion proceeds through successive stages until the fully lithiated LiC_6 phase is formed (Sole et al., 2014). In parallel, crystalline silicon gradually transformed into amorphous Li_xSi. Comparing the charge–discharge profiles of the electrodes containing different binders at higher C-rates (Fig. 4c–f,i), as mentioned before, the ALG-based electrode retains higher capacity at 2C, exhibiting a more pronounced CC discharge contribution compared to CMC and TG. Despite these differences, it is important to emphasize that CMC, even though always paired with SBR in industrial formulations and used by itself in this work as a reference material, is a binder specifically optimised for large-scale LIBs production. Therefore, the electrochemical performances achieved with ALG and TG remain highly promising, as they do not significantly deviate from those observed for the CMC-based electrodes. Table S3 summarises the average electrochemical performance of all the tested electrodes.

Concerning the ICE, all samples exhibited values below 85 % (Fig. 4j), likely due to some initial irreversible reaction and the formation of the solid electrolyte interphase and a consequent lithium loss during the first cycle (Ravesio et al., 2025; Sun et al., 2022). Analysing the subsequent cycles, all electrodes exhibited a progressive increase in Coulombic efficiency (CE), confirming the gradual forming process of the cells and overall system stabilisation. Notably, by the fifth cycle, the CE of the CMC-based electrodes exceeded 95%, indicating the best electrochemical performance among the samples at this initial stage. However, starting from the 15th cycle, electrodes incorporating TG exhibit the most promising results, maintaining excellent CE values even under high C-rate conditions. This improved performance is likely attributed to the hydroxyl and carboxyl groups present in the TG binder, which interact with the SiO_x particles and enhance structural stability. More in general, after the initial formation cycles, the CE values of electrodes containing ALG and TG become higher, either comparable to (ALG) or slightly exceeding (TG) those of the CMC-based reference electrode. These results demonstrate that both ALG and TG binders enable excellent electrochemical performance.

The direct comparison of different polysaccharide-based binders identified ALG as the most promising candidate, owing to its favourable rheological behaviour and significant electrochemical performance. To further enhance these advantages, a binary mixture of ALG and LiPAA was evaluated. This strategy aimed to synergistically combine the advantages of both binders, harnessing the mechanical stability and electrochemical performances of ALG together with the strong adhesion and additional lithium-ion contribution provided by LiPAA.

To gain a broader overview of the synergistic effect between ALG and LiPAA, three binder weight ratios (*i.e.*, 1_{LiPAA}:2_{ALG}, 1_{LiPAA}:1_{ALG}, and 2_{LiPAA}:1_{ALG}) were selected. These compositions represent equidistant mixture points within the experimental design space, allowing for a systematic and balanced exploration of the combined effects of the two binders. The characterisation procedure applied to these electrodes followed the same methodology previously described, with additional tests detailed in the Supporting Information (Figs. S4–S8 and Tables S4–S9).

FT-IR analysis was performed on all binders, both in their pure form and in mixtures (1:2, 1:1, and 2:1), in order to confirm the presence of the key functional groups able to interact with the active material. The resulting spectra are reported in Fig. 5 and the corresponding band in Table S4. All samples exhibit a broad band in the 3500–3200 cm^{-1} region, attributable to –OH stretching and adsorbed water. In this frequency region, sodium alginate shows a more intense contribution, indicating a higher density of hydrogen bonds or free hydroxyl groups. In the 3000–2850 cm^{-1} range, a weak band associated with C–H stretching is observed for all the samples. The most significant difference can be observed in the region within 1650–1400 cm^{-1}, associated with carboxylates (1600–1650 cm^{-1}: asymmetric stretching, 1400–1450 cm^{-1}: symmetric stretching of the COO^-). The presence of both symmetric and asymmetric COO^- bands in all LiPAA-containing samples confirms a high degree of polymer lithiation, further supported by the absence of the characteristic –COOH band at 1700 cm^{-1}. In this region, ALG displays two well-defined, intense bands, whereas the mixed binders exhibit less pronounced and slightly shifted bands. The fingerprint region (1300–1000 cm^{-1}) is markedly more complex for sodium alginate, reflecting the polysaccharide structure through multiple C–O and C–O–C vibrations. These bands become progressively less intense as the LiPAA content in the mixtures increases (Hu et al., 2021). As mentioned before, for the asymmetric and symmetric COO^- stretching modes, the binders mixtures show peak positions between those of pure ALG and pure LiPAA. The calculation of the frequency difference $\Delta\nu$ between these two vibrational modes provides further insight: ALG exhibits a larger $\Delta\nu$ (185 cm^{-1}), LiPAA the lower $\Delta\nu$ (141 cm^{-1}), while all binders mixtures fall in between, but progressively tend toward the LiPAA value. This behaviour suggests a more symmetric coordination environment for the COO^- groups, likely involving bidentate or bridging binding to Li^+, which results in a more uniform electron distribution between the two oxygen atoms. In conclusion, these observations support the hypothesis of a possible homogeneous ionic crosslinking in the mixtures, potentially enhancing resistance to volumetric changes in the anode. The FT-IR analysis indicates a possible chemical–physical interaction between the two binders, consistent with good miscibility and mutual interaction within the mixed formulation (Sharratt et al., 2021).

Fig. 6 reports the rheological characterisation of the slurries prepared with the binder mixtures and the pure binders (ALG and LiPAA). Because of LiPAA highly fluid behaviour and inherently low viscosity, both as a binder solution (Fig. S4a and b) and in the anodic slurry, the pure LiPAA slurry and its mixtures exhibited uniformly low viscosity across the entire shear-rate range (Fig. 6a). The shear-thickening behaviour seen in the LiPAA system, and to a lesser extent in the mixtures, is attributed to the aggregation of carbon black and SiO_x/C particles, which tend to significantly agglomerate in aqueous media due to their small size (Lim et al., 2015). In the case of pure LiPAA, the binder lacks sufficient cohesive strength to effectively disperse and stabilize the active and conductive materials. Consequently, the rheological response is not a binder-induced shear-thickening effect, but rather a result of particle agglomeration. Furthermore, the suspension exhibited poor resting stability, as this type of binder allowed phase segregation and particle settling over time (He et al., 2022; Lee et al., 2010). As shown in Fig. 6b–e, all the slurries exhibit a behaviour characterised by frequency-independent G' and G'' moduli over a wide frequency range. The magnitude of G' and G'' is significantly higher for the mixtures, while pure LiPAA slurry displays markedly lower moduli. This response is not due to the intrinsic viscosity of the binders, but rather to the previously discussed agglomeration effects.

The resulting flow curves were fitted using a time-irrelevant Herschel-Bulkley model, and the error R^2 was used to evaluate the yield stress obtained by the extrapolation of flow curves in the model.

$$\tau = \tau_0 + K(\gamma)n \qquad \text{Eq. 1}$$

where τ is the shear stress (Pa), τ_0 is the yield stress (Pa), K is the consistency coefficient (Pa·s^n), γ is the shear rate (s^{-1}), and n is the flow

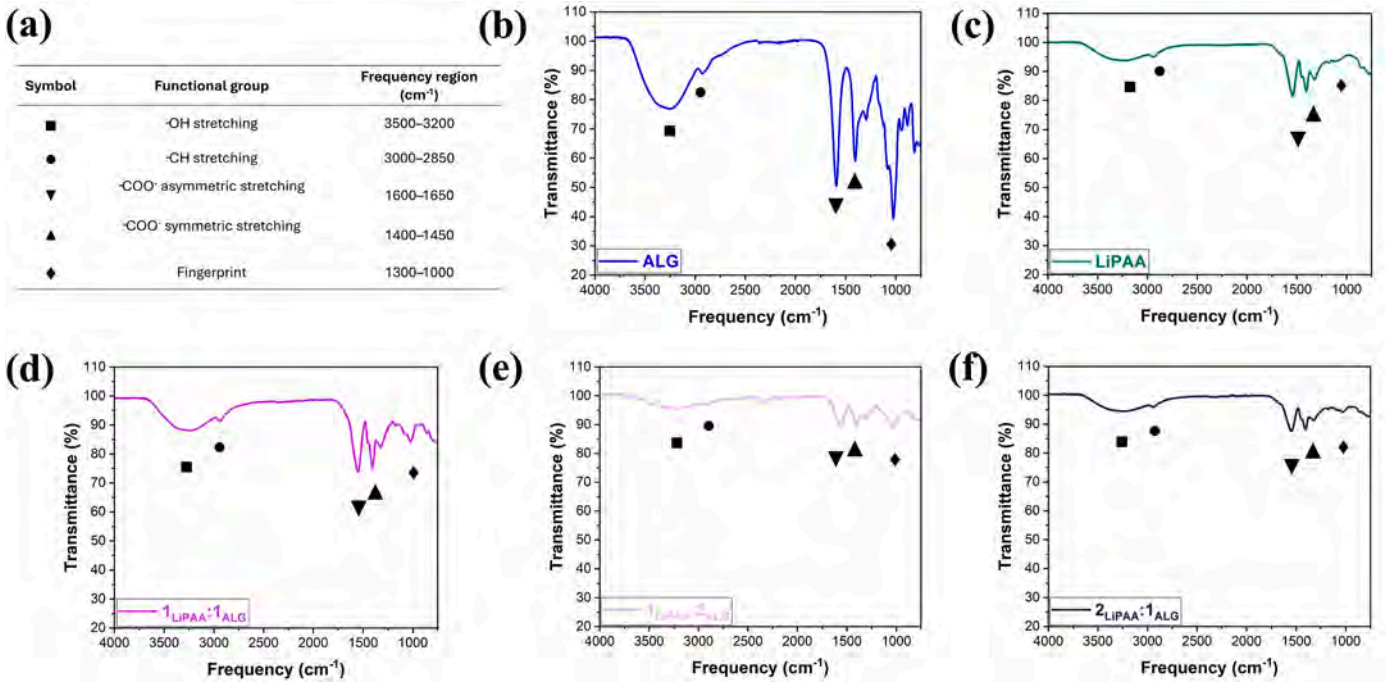


Fig. 5. Major functional group and corresponding frequency range (a). FT-IR spectra of ALG (b), LiPAA (c), 1_{LiPAA}:1_{ALG} (d), 1_{LiPAA}:2_{ALG}, (e) 2_{LiPAA}:1_{ALG} (f).

behaviour index (dimensionless) (Zhao et al., 2022).

The parameters, reported in Table S5, show a clear distinction between slurries with a predominance of sodium alginate (or with equal ALG and LiPAA amount) and those with a predominance of LiPAA. Slurries containing pure ALG as well as the 1_{LiPAA}:1_{ALG} and 1_{LiPAA}:2_{ALG} mixtures exhibit $\tau_0 = 0$. Therefore, according to the Herschel-Bulkley model, they do not display a measurable yield stress. In contrast, slurries containing pure LiPAA and the 2_{LiPAA}:1_{ALG} mixture show a $\tau_0 \approx$ 4–5.5 Pa, indicating the presence of a more elastic microstructure that requires a minimum stress threshold to start the flow. The consistency index K, which is considered a measure of viscosity, increases with the ALG fraction in the formulation: LiPAA < 2_{LiPAA}:1_{ALG} < 1_{LiPAA}:1_{ALG} < 1_{LiPAA}:2_{ALG} < ALG. Therefore, ALG dominates the consistency and makes the slurry more viscous, while binder mixtures allow for effective viscosity modulation, especially at low shear. Flow index n, shows an inverse trend, confirming that the higher amount of ALG in the slurry leads to a more marked shear-thinning behaviour and consequently a better fluidization at high shear rates. For all slurries containing LiPAA, the fitting quality is good, with $R^2 > 0.995$. Only ALG exhibits a slightly lower value ($R^2 \approx 0.994$), which is consistent with its higher structural complexity. Overall, the Herschel-Bulkley model provides a satisfactory description of the rheological behaviour of all slurries. In conclusion, according to rheological results, LiPAA-based slurries require less effort for coating, while ALG-based slurries are the most structured, viscous, and exhibit greater shear-thinning behaviour. The mixing of the two binders allows for yield stress, viscosity, and shear-thinning adjustment, according to the formulation.

Regarding the mass loading (ML) distribution (Fig. S5), the electrodes containing ALG and LiPAA show similar average ML values. However, the LiPAA-based electrodes exhibit slightly lower variability, suggesting a more uniform binder distribution during the mixing process and the subsequent coating. Similarly, for the three binder mixtures, the variability appears relatively low, and the ML values consistently fall within a comparable range.

The morphological analysis of the electrodes containing different binder mixtures (Fig. S6) confirmed the observations made for electrodes prepared using the single binders, as a good distribution of the active material and carbon black particles is observable. These results support the consideration that the combination of ALG and LiPAA does not significantly alter the electrode morphology.

Regarding the electrochemical properties, the cyclic voltammetry profiles of the electrodes containing different binder mixtures show behaviours similar to those observed for electrodes with pure ALG and LiPAA. As reported in Fig. S7, a progressive stabilisation of the CV profiles is observed from the first to the fifth cycle, which can be attributed to the gradual activation of the active material and the amorphisation of the silicon phase. The same considerations applied to pure ALG-based electrodes can also be extended to the other sample, where peaks are observed during the cathodic scan at 0.17 V and 0.02 V, and during the anodic scan between 0.16 V and 0.25 V, with an additional peak at 0.5 V. As the cycling progresses (by the 5th cycle), these peaks slightly shift towards higher potentials. However, it is important to highlight that the CV profiles of the different electrodes largely overlap, with no significant evidence of overpotential or polarization phenomena. This suggests good compatibility between the binders and their mixtures with the active material.

Fig. 7a shows the electrochemical results of the rate capability test for the electrodes with the three different binder formulations, directly compared with the electrodes containing every single binder. In general, LiPAA-based electrodes showed better average capacity in the initial cycles at C/10 than ALG-based ones (422.3 mAh/g vs. 414.7 mAh/g), as reported in Table 1. At the same time, the two mixtures, 1_{LiPAA}:2_{ALG} and 1_{LiPAA}:1_{ALG}, exhibited intermediate properties. On the contrary, the electrodes with a binder weight ratio of 2_{LiPAA}:1_{ALG} exhibited enhanced electrochemical performance. In particular, the electrodes with this formulation demonstrated better long-cycling stability, achieving an average charge capacity of 336.8 mAh/g by the 30th cycle. In Fig. 7b, the average CE at several defined cycles is shown. Electrodes based on the binder mixtures exhibited improved performance, primarily due to the presence of LiPAA, which enhanced the initial cycle efficiency, reaching over 85% already from the ICE. This improvement was attributed to the higher ionic conductivity and the formation of a stable SEI layer during the early cycles. Analogously, from the charge-discharge curves, it was observed that the most representative 2_{LiPAA}:1_{ALG} mixture electrode (Fig. 7g and h) exhibited a well-defined average specific capacity during forming cycles and lower initial

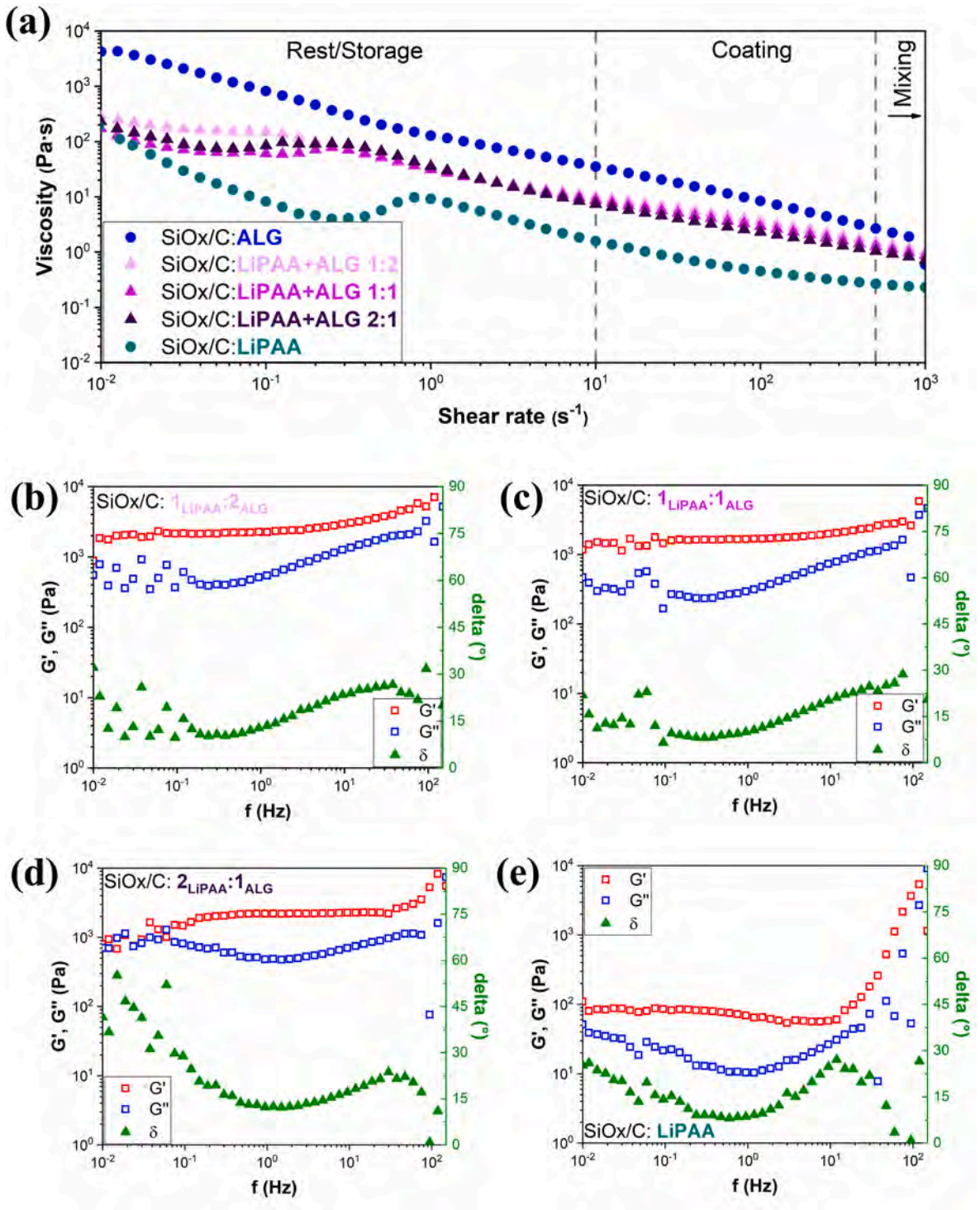


Fig. 6. Viscosity profiles of all slurries as a function of shear rate (a), and frequency sweep test results for SiOx/C: 2_{LiPAA}:1_{ALG} (b), 1_{LiPAA}:1_{ALG} (c), 1_{LiPAA}:2_{ALG} (d), and LiPAA (e).

capacity loss, with a reduced polarization between the anodic and cathodic voltage profiles. At the same time, electrodes with 2_{LiPAA}:1_{ALG} mixture showed better capacity retention, attributable to good mechanical stability, guaranteed by the presence of ALG in the electrode formulation. In conclusion, among the tested compositions, the electrodes with 2_{LiPAA}:1_{ALG} mixture appeared to lead to significant performance improvements. Therefore, the rational combination of LiPAA and ALG likely contributes to the formation of a more stable SEI layer, while simultaneously ensuring an enhanced adhesion and better ion transport, driven by the formation of hydrogen and ionic bonds. This effect would be crucial in improving the long-term performance of the battery, further explaining the superior cyclability observed with this binder ratio (Qin et al., 2024).

To better evaluate the influence of different binder formulations on the cell internal resistance, PEIS analyses were performed on the different samples. All PEIS measurements were acquired under relaxation conditions. Fig. 8 shows the corresponding Nyquist plots, highlighting the evolution of the total internal resistance after three

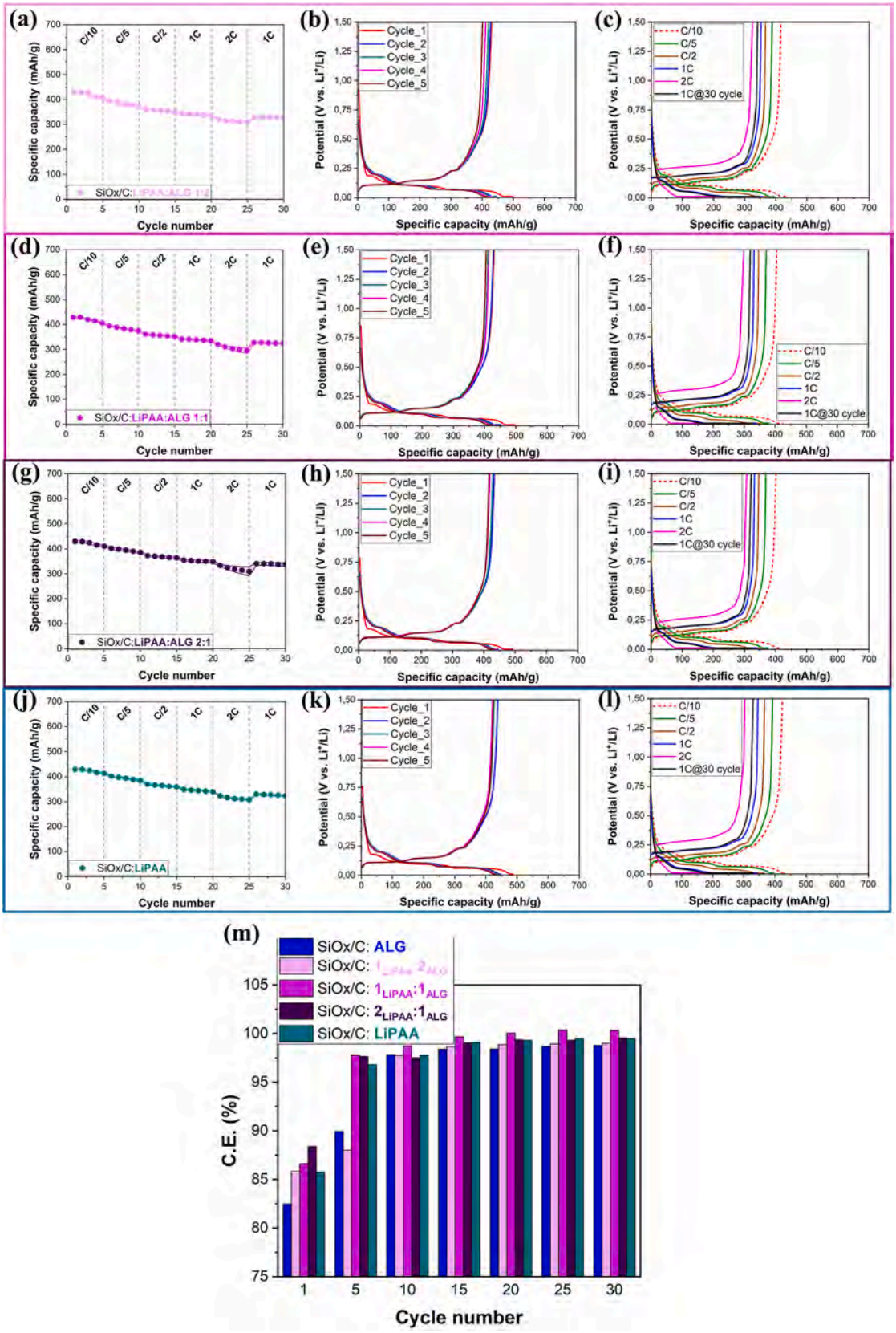


Fig. 7. (a) Average specific capacity of electrodes with pure and mixtures of binders (a,d,g,j), measured up to 30 cycles, charge and discharge profiles during the forming cycles and at different C-rates for the most representative electrodes containing: 1_{LiPAA}:2_{ALG} (b,c), 1_{LiPAA}:1_{ALG} (e,f), 2_{LiPAA}:1_{ALG} (h,i), and LiPAA (k,l). Average CE of electrodes with pure and mixtures of binders, measured up to 30 cycles (m).

Table 1
Summary of the average specific charge capacity, capacity retention, and CE at different cycles for the rate capability test and the first long cycling protocol of SiO_x/C electrodes with different binders and binder mixtures (the first number represents the LiPAA content and the second represents the ALG content).

C-rate	Specific capacity (mAh/g)					Capacity retention (%) ref. av. C/10					CE (%)				
	ALG	LiPAA	1:2	1:1	2:1	ALG	LiPAA	1:2	1:1	2:1	ALG	LiPAA	1:2	1:1	2:1
C/10	414.7	422.3	420.1	419.6	421.3	-	-	-	-	-	88.6	92.4	90.5	94.6	95.8
C/5	371.5	392.9	382.9	383.9	394.0	89.6	93.0	91.1	91.5	93.5	97.5	98.0	97.4	98.4	97.3
C/2	346.7	363.8	355.8	356.1	368.0	83.6	86.1	84.7	84.9	87.3	98.3	98.9	98.3	99.4	98.9
1C	330.9	343.8	339.9	338.2	351.1	79.8	81.4	80.9	80.6	83.3	98.4	99.1	98.5	99.9	99.4
2C	309.3	313.7	313.7	305.3	319.8	74.6	74.3	74.7	72.8	75.9	98.5	99.3	98.8	100	99.3
1C*30 cycle	318.4	326.7	328.2	325.6	338.9	76.8	77.4	78.1	77.6	80.4	98.8	99.8	99.0	100	99.7

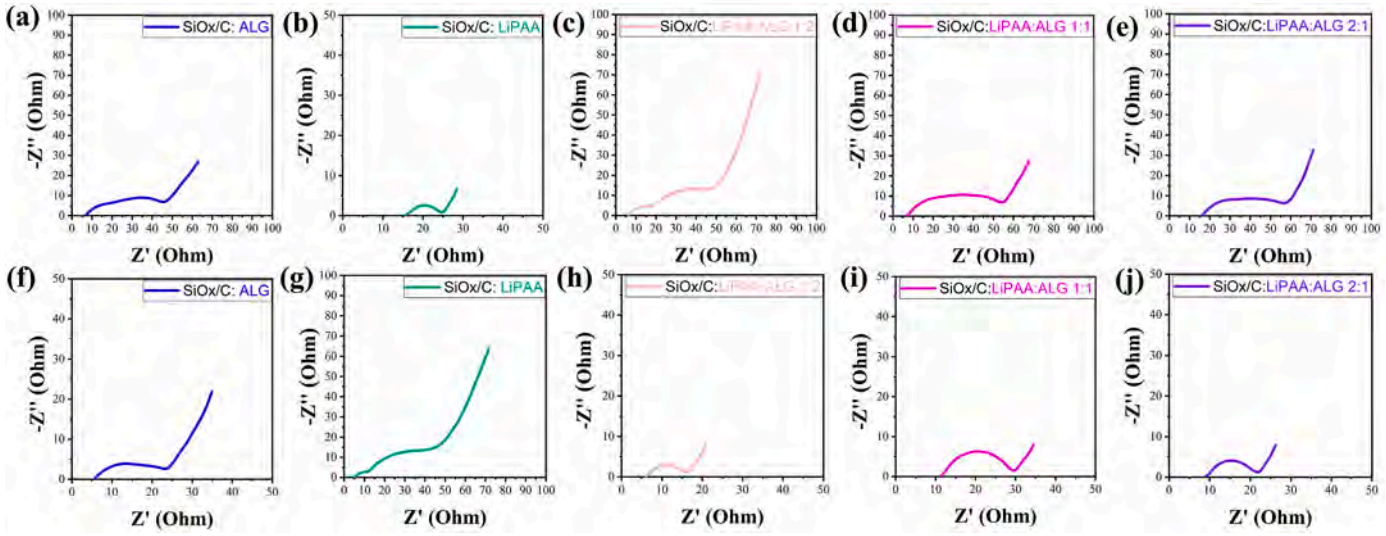


Fig. 8. Nyquist plots after three formation cycles at C/10 (a-e) and after the rate capability test (f-j), respectively for electrode containing: ALG, LiPAA, 1_{LiPAA}:2_{ALG} mixture, 1_{LiPAA}:1_{ALG}, and 2_{LiPAA}:1_{ALG}.

formation cycles at C/10 and after the rate capability (RC) test. Table S7 summarises the PEIS parameters obtained by fitting the data using the equivalent circuit model (ECM) reported in Scheme S1. The proposed ECM (scheme S1) includes the bulk resistance (R_{el}), representing the intrinsic resistance of the bulk materials/wires/current collector/electrolyte, the SEI layer resistance (R_{SEI}), the charge-transfer resistance (R_{ct}), and the semi-infinite diffusion (W). All Nyquist plots can be deconvoluted into two semicircles, corresponding to the resistance of the SEI film (high-frequency region) and the charge-transfer resistance (mid-frequency region), respectively. From both the Nyquist plots and the fitted parameters (Table S7), no clear trend can be attributed to the amount of one binder over the other, contained in the mixture. In particular, after the initial three cycles at C/10, all samples exhibit a profile in which the two contributions, R_{SEI} and R_{ct}, remain clearly distinguishable. However, the Nyquist profiles become more distinct after the cycling at various C-rates (RC test). In this case, the electrode containing sodium alginate exhibits a visibly different impedance response compared to the electrodes containing pure LiPAA or binder mixture. Notably, for ALG-based electrodes, the high-frequency semicircle associated with R_{SEI} is the main contribution to the total resistance, exceeding the semicircle related to the charge-transfer resistance. In contrast, for electrodes with pure or mixed LiPAA, the resistance associated with the SEI layer remains consistently lower than the charge-transfer resistance. This behaviour highlights the difference in the functional role of the two binders (LiPAA and ALG), and it is consistent with the trends observed for the initial coulombic efficiency (ICE), which is higher when LiPAA is present in the binder formulation. More in detail, after the initial formation cycles, the electrode containing pure LiPAA exhibits a lower R_{SEI} than the electrode formulated with pure sodium alginate, confirming that LiPAA promotes the formation of a less resistive SEI layer. The reduced R_{SEI} observed for the pure-LiPAA electrode supports the hypothesis that LiPAA contributes to the formation of a protective artificial SEI layer on the surface of graphite/SiO_x composite anodes, preserving the structural integrity of the SEI during cycling, as also reported in previous works (Truong et al., 2021). Indeed, the molecular structure of sodium alginate promotes the formation of a thicker SEI film. However, the higher R_{SEI} observed for the ALG-based electrode is compensated by a lower R_{ct}, resulting from its stronger binding capability, which ensures improved mechanical cohesion and better contact among the active material particles (Güneren et al., 2024; Dong et al., 2025). As reported by Hu et al., the higher initial R_{ct} observed for the electrode containing the binder mixture may be attributed to LiPAA domains occupying the cavities within the sodium alginate network, which can partially hinder the ionic transfer (Hu et al., 2021). In general, more significant and conclusive insights can be drawn by examining the R_{tot} ($R_{SEI} + R_{ct}$) value and comparing it after the first three cycles at C/10 and following the RC test. In this regard, it is evident that electrodes containing pure LiPAA, as well as those incorporating 1_{LiPAA}:2_{ALG} and 2_{LiPAA}:1_{ALG} binder mixtures, exhibit lower total resistance than both pure alginate and the 1_{LiPAA}:1_{ALG} mixture.

Thus, to better evaluate the influence of the optimised binder mixture on the electrochemical properties of the cell, a long-cycling behaviour was also investigated (Fig. 9). From Fig. 9a, it can be observed that LiPAA-based electrodes confirmed a higher ICE and reduced capacity loss, as expected. However, during long-term cycling, performance issues emerged, probably due to the higher mechanical fragility of the LiPAA binder compared to ALG. In contrast, ALG-based electrodes demonstrated better capacity retention, maintaining 49.5 % of the average capacity measured at the 10th cycle after 300 cycles (as reported in Table 2), thanks to the stronger adhesion between the active

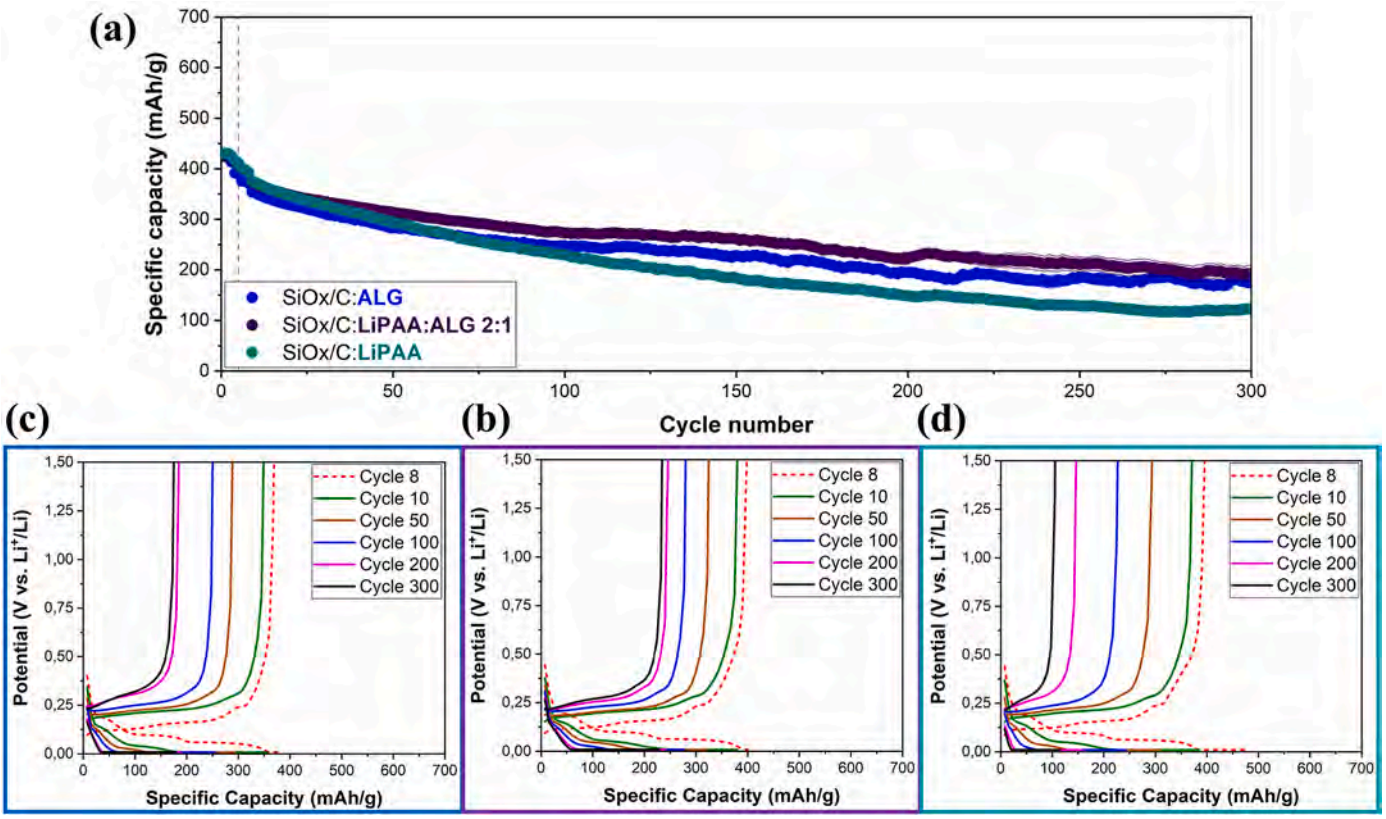


Fig. 9. Long-term cycling protocol for electrodes containing ALG, 2_{LiPAA}:1_{ALG}, and LiPAA binders (a), and charge-discharge profiles of the most representative cells with ALG (b), 2_{LiPAA}:1_{ALG} (c), and LiPAA (d).

Table 2
Summary of the average specific charge capacity, capacity retention, and CE at different cycles for the second long cycling protocol of SiO_x/C electrodes with the two guideline binders and the best-performing binder mixture.

Cycle number	Specific capacity (mAh/g)			Capacity retention (%) ref. (Liu et al.)th cycle (%)			CE (%)		
	LiPAA	2_{LiPAA}:1_{ALG}	ALG	LiPAA	2_{LiPAA}:1_{ALG}	ALG	LiPAA	2_{LiPAA}:1_{ALG}	ALG
1st C/10	430.6	424.4	425.7	-	-	-	84.4	86.2	89.2
2nd C/10	430.2	425.5	422.2	-	-	-	92.2	95.4	97.2
3rd C/10	425.7	422.6	413.3	-	-	-	94.4	97.5	97.4
8th C/5	392.6	392.2	371.4	-	-	-	95.7	98.2	98.9
10th 1C	372.4	370.2	351.9	-	-	-	99.3	99.3	99.6
50th 1C	293.0	313.7	283.5	78.7	84.7	80.6	99.6	100	100
100th 1C	229.7	272.8	247.9	61.7	73.7	70.4	99.4	100	100
200th 1C	148.2	222.6	194.6	39.8	60.1	55.3	100	100	100
300th 1C	122.0	192.8	174.1	32.8	52.1	49.5	100	100	100

material and better mechanical properties ascribable to ALG. However, the electrodes incorporating the mixture 2_{LiPAA}:1_{ALG} exhibited high average specific capacity and improved capacity retention, showing the lowest polarization and the best overall electrochemical performance, if compared with the electrode with pure ALG or LiPAA. This confirms once again that the combination of the two binders has an improving effect on the electrochemical properties of the SiO_x/C electrode, and that each binder contributes synergistically to this enhancement.

Hence, to confirm the combined effect of LiPAA and ALG in the electrode formulation a simple linear regression and one-way ANOVA were used to analyse the influence of the percentage of LiPAA on cell capacity at the 5th (C/10), 10th (C/5), 15th (C/2), 20th (1C), 25th (2C), and 50th (1C) cycles, based on the data presented in Fig. 10 and Table S9. The dataset consisted of three electrodes for every single binder (LiPAA, ALG) and their respective mixtures (1_{LiPAA}:2_{ALG}, 1_{LiPAA}:1_{ALG} and 2_{LiPAA}:1_{ALG}). The analysis was performed by considering one independent variable at a time (*i.e.*, the weight percentage of LiPAA). Obviously, the percentage of LiPAA and the complementary percentage of ALG exhibited multicollinearity, and therefore, they were considered as a single factor in the model. Observing the results reported in Table S9 cycles 5, 10, and 15 (at C/10, C/5, and C/2, respectively) exhibit a low MSW, indicating limited variability in the data. At the same time, the high F values and $p < 0.05$ confirm a significant effect of the LiPAA binder. At cycle 20 (1C), the MSW remains low, while the moderate F value and $p \approx 0.05$ suggest that the binder effect is still statistically relevant. On the contrary, at cycle 25, corresponding to high C-rates (2C), the MSW becomes very high, indicating a greater dispersion of the capacity values. The p and F values show that no appreciable differences attributable to the binders are present under these conditions. By cycle 50, after additional 25 cycles at a fixed rate of 1C, the data dispersion remains high and does not support a significant role of LiPAA, suggesting that the influence of this binder becomes less appreciable

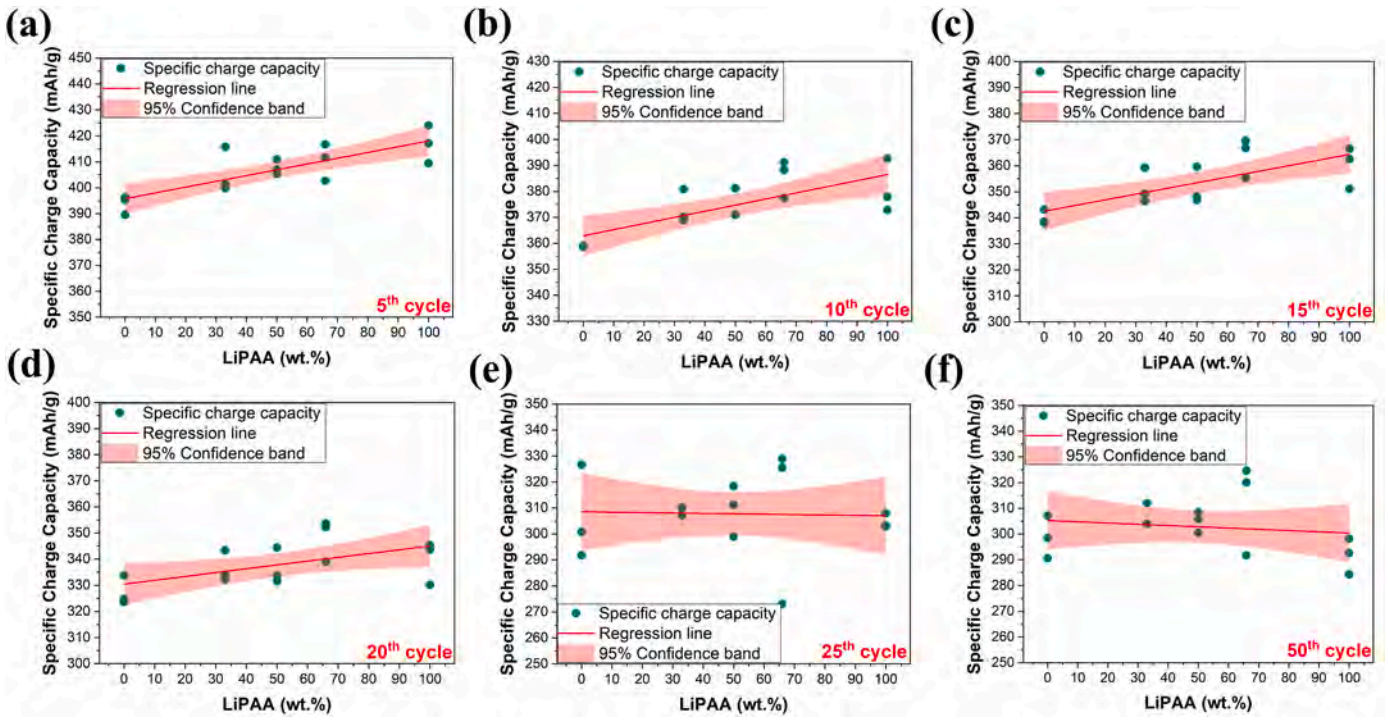
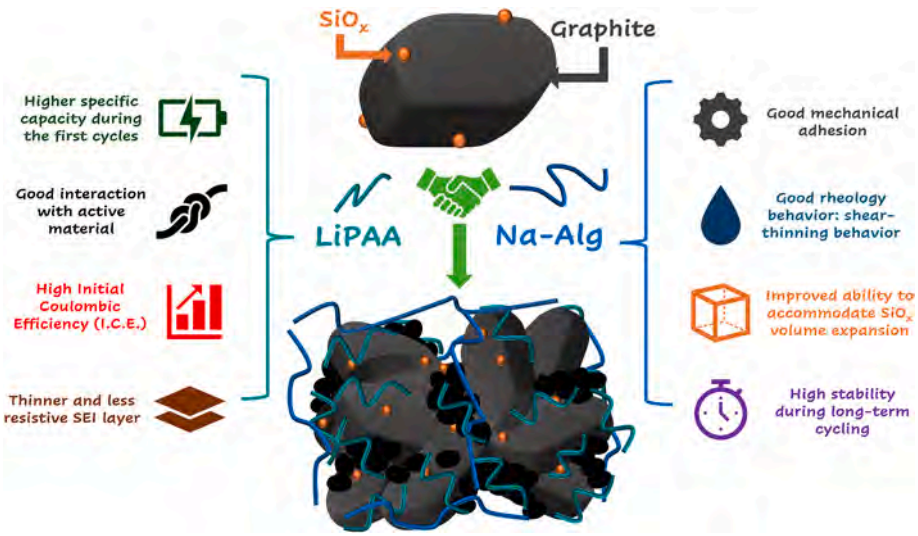


Fig. 10. Simple linear regression of the percentage of LiPAA in the mixture influencing specific charge capacity at the 5th (a), 10th (b), 15th (c), 20th (d), 25th (e), and 50th cycles (f).

increasing the number of cycles. In summary, the binder effect is evident in the early stages of cycling at lower C-rates (5 to 15 cycles), where LiPAA significantly increases the specific capacity. As the C-rate and number of cycles increase, the effect tends to diminish until it becomes progressively undetectable up to 50 cycles, where no significant differences emerge. The effect size (Table S9) confirms that the binder has a clear influence in the first cycles and at lower C-rates, progressively decreasing between cycles 20 and 25, *i.e.* at higher C-rates. At the end of the 50 cycles, the binder effect remains qualitatively present, but less statistically significant. The observed trend suggests that the presence of LiPAA significantly improves the cell initial capacity, while sodium alginate better supports long-term structural stability. These results are consistent with LiPAA ability to enhance the initial charge-discharge cycles capacity and reversibility of SiO_x/C composite electrodes, as previously reported by Truong et al. (2021). LiPAA forms a stable artificial SEI layer, minimising irreversible lithium loss. As an ion-conductive polymer, it helps compensate for lithium loss and facilitates ion transport (Pieczonka et al., 2015; Li et al., 2010). However, the combination with other complementary binders (such as ALG), according to rational and optimised ratios, is fundamental to improve the mechanical stability of the electrode and improve the capacity retention over a high number of cycles. For these reasons LiPAA:ALG binder mixture confirms to be the best overall compromise (Scheme 1). A comparative table with more relevant literature studies is reported in SI (Table S10).



Scheme 1. Effect of LiPAA and ALG in SiO_x/C electrode.

4. Conclusions

This study aimed to investigate the use of alternative water-based binders and their rational combination through simple blending strategies for the manufacturing of SiO_x/C electrodes. The work focused on screening different polymer binders, evaluating their electrochemical performance and processability, to identify the most suitable options, balancing sustainability, performance, and manufacturability. Throughout the study, parameters such as slurry formulation, solid content, coating thickness, and cell assembly conditions were carefully controlled to ensure comparability of the results. Among the tested binders, ALG showed excellent compatibility, with favourable pH values, good rheological behaviour, and electrochemical performance. For this reason, ALG was selected for further investigation in combination with LiPAA. Regarding the binder mixtures, the formulation 2_{LiPAA}:1_{ALG} demonstrated better electrochemical properties, achieving high specific capacity, excellent CE, and good capacity retention over cycling. Through an accurate data analysis, supported by a statistical study, LiPAA showed a huge contribution to enhance the ICE, while ALG contributed to a better long-term capacity retention. Overall, the results highlight the potential of combining natural polysaccharide-based binders with synthetic binders like LiPAA to balance sustainability, mechanical integrity, and electrochemical performance of LIB anodes. Nevertheless, further rheological optimization will be necessary to fully exploit these binder systems for industrial application in next-generation LIBs.

CRediT authorship contribution statement

Lorenzo Tamboia: Writing – original draft, Visualization, Methodology, Investigation, Data curation. **Giorgio Montinaro:** Writing – review & editing, Validation, Methodology, Investigation, Data curation, Conceptualization. **Elisa Ravesio:** Writing – review & editing, Validation, Methodology, Conceptualization. **Julia Amici:** Writing – review & editing, Validation, Methodology, Investigation. **Carlotta Francia:** Writing – review & editing, Funding acquisition. **Silvia Bodoardo:** Writing – review & editing, Resources, Funding acquisition. **Federico Bella:** Writing – review & editing, Supervision, Resources. **Daniele Versaci:** Writing – original draft, Visualization, Validation, Supervision, Methodology, Data curation, Conceptualization.

Declaration of competing interest

The authors declare that they have no known competing financial interests or personal relationships that could have appeared to influence the work reported in this paper.

Acknowledgements

The authors would like to thanks “Network 4 Energy Sustainable Transition” - NEST, -Piano Nazionale di Ripresa e Resilienza (PNRR), M4C2 Spoke 6– NextGenerationEU financed by the European Union, for the financial support.

Appendix A. Supplementary data

Supplementary data to this article can be found online at https://doi.org/10.1016/j.jclepro.2026.148153.

Data availability

Data will be made available on request.

References

Abel, P.R., Lin, Y.M., Celio, H., Heller, A., Mullins, C.B., 2012. Improving the stability of nanostructured silicon thin film lithium-ion battery anodes through their controlled oxidation. ACS Nano 6, 2506–2516. https://doi.org/10.1021/nn204896n.

B.L. Armstrong, K.A. Hays, R.E. Ruther, W.B. Hawley, A. Rogers, I. Greeley, K.A. Cavallaro, G.M. Veith, K.A. Hays, G.M. Veith, A. Rogers, I. Greeley, R.E. Ruther, W.B. Hawley, K.A. Cavallaro, Role of Silicon-Graphite Homogeneity as Promoted by Low Molecular Weight Dispersants, n.d.

Bresser, D., Buchholz, D., Moretti, A., Varzi, A., Passerini, S., 2018. Alternative binders for sustainable electrochemical energy storage-the transition to aqueous electrode processing and bio-derived polymers. Energy Environ. Sci. 11, 3096–3127. https://doi.org/10.1039/c8ee00640g.

Chen, Y., Guo, F., Yang, L., Lu, J., Liu, D., Wang, H., Zheng, J., Yu, X., Li, H., 2022. Probing component contributions and internal polarization in silicon-graphite composite anode for lithium-ion batteries with an electrochemical-mechanical model. Chin. Phys. B 31. https://doi.org/10.1088/1674-1056/ac6012.

Chou, W.Y., Jin, Y.C., Duh, J.G., Lu, C.Z., Liao, S.C., 2015. A facile approach to derive binder protective film on high voltage spinel cathode materials against high temperature degradation. Appl. Surf. Sci. 355, 1272–1278. https://doi.org/10.1016/j.apsusc.2015.08.046.

Cuesta, N., Ramos, A., Cameán, I., Antuña, C., García, A.B., 2015. Hydrocolloids as binders for graphite anodes of lithium-ion batteries. Electrochim. Acta 155, 140–147. https://doi.org/10.1016/j.electacta.2014.12.122.

Dang, D., Wang, Y., Wang, M., Hu, J., Ban, C., Cheng, Y.T., 2020. Lithium substituted Poly(acrylic acid) as a mechanically robust binder for low-cost silicon microparticle electrodes. ACS Appl. Energy Mater. 3, 10940–10949. https://doi.org/10.1021/acsaem.0c01923.

Dong, B., Zhu, H., Cai, X., Guo, C., Hao, Y., Xi, L., 2025. Rational design of alginate-derived network binder for high-performance silicon-based anodes in Li-ion batteries. J. Power Sources 626. https://doi.org/10.1016/j.jpowsour.2024.235745.

Drofenik, J., Gaberscek, M., Dominko, R., Poulsen, F.W., Mogensen, M., Pejovnik, S., Jamnik, J., 2003. Cellulose as a binding material in graphitic anodes for Li ion batteries: a performance and degradation study. Electrochim. Acta 48, 883–889. https://doi.org/10.1016/S0013-4686(02)00784-3.

Dühnen, S., Betz, J., Kolek, M., Schmuch, R., Winter, M., Placke, T., 2020. Toward green battery cells: perspective on materials and technologies. Small Methods 4. https://doi.org/10.1002/smtd.202000039.

Golombek, R., Lind, A., Ringkjøb, H.K., Seljom, P., 2022. The role of transmission and energy storage in European decarbonization towards 2050. Energy 239. https://doi.org/10.1016/j.energy.2021.122159.

Güneren, A., Nada, A.A., Šišková, A.O., Mosnáčková, K., Kleinová, A., Mosnáček, J., Lenčéš, Z., 2024. Novel alginate-based binders for silicon–graphite anodes in lithium-ion batteries: effect of binder chemistry on the electrochemical performance. J. Appl. Electrochem. 54, 1409–1423. https://doi.org/10.1007/s10800-023-02038-z.

Guo, R., Zhang, S., Ying, H., Yang, W., Wang, J., Han, W., 2019. Preparation of an amorphous cross-linked binder for silicon anodes. ChemSusChem 12, 4838–4845. https://doi.org/10.1002/cssc.201902079.

He, Y., Jing, L., Ji, Y., Zhu, Z., Feng, L., Fu, X., Wang, Y., 2022. Revisiting the electrode manufacturing: a look into electrode rheology and active material microenvironment. J. Energy Chem. 72, 41–55. https://doi.org/10.1016/j.jechem.2022.04.038.

Hu, Y.Y., You, J.H., Zhang, S.J., Lin, H., Ren, W.F., Deng, L., Pan, S.Y., Huang, L., Zhou, Y., Li, J.T., Sun, S.G., 2021. Li0.5PAA domains filled in porous sodium alginate skeleton: a 3D bicontinuous composite network binder to stabilize micro-silicon anode for high-performance lithium ion battery. Electrochim. Acta 386. https://doi.org/10.1016/j.electacta.2021.138361.

Jang, W., Rajeev, K.K., Thorat, G.M., Kim, S., Kang, Y., Kim, T.H., 2022. Lambda carrageenan as a water-soluble binder for silicon anodes in lithium-ion batteries. ACS Sustain. Chem. Eng. 10, 12620–12629. https://doi.org/10.1021/acssuschemeng.2c03313.

Kasinathan, R., Marinaro, M., Axmann, P., Wohlfahrt–Mehrens, M., 2018. Influence of the molecular weight of poly-acrylic acid binder on performance of Si-Alloy/Graphite composite anodes for lithium-ion batteries. Energy Technol. 6, 2256–2263. https://doi.org/10.1002/ente.201800302.

Kim, S.O.N.H., Waldhoff, S.T., Edmonds, J.A., 2023. THE ROLE of BATTERY ELECTRIC VEHICLES in DEEP DECARBONIZATION. Clim. Chang. Econ. (Singap). 14. https://doi.org/10.1142/S2010007823500045.

Kovalenko, I., Zdyrko, B., Magasinski, A., Hertzberg, B., Milicev, Z., Burtovyy, R., Luzinov, I., Yushin, G., 1979. A major constituent of brown algae for use in high-capacity Li-ion batteries. Science 334 (2011), 75–79. https://doi.org/10.1126/science.1209150.

Lai, Y., Li, H., Yang, Q., Li, H., Liu, Y., Song, Y., Zhong, Y., Zhong, B., Wu, Z., Guo, X., 2022. Revisit the progress of binders for a silicon-based anode from the perspective of designed binder structure and special sized silicon nanoparticles. Ind. Eng. Chem. Res. 61, 6246–6268. https://doi.org/10.1021/acs.iecr.2c00453.

Lee, G.W., Ryu, J.H., Han, W., Ahn, K.H., Oh, S.M., 2010. Effect of slurry preparation process on electrochemical performances of LiCoO2 composite electrode. J. Power Sources 195, 6049–6054. https://doi.org/10.1016/j.jpowsour.2009.12.101.

Legerstee, W.J., Noort, T., van Vliet, T.K., Schut, H., Kelder, E.M., 2022. Characterisation of defects in porous silicon as an anode material using positron annihilation Doppler Broadening spectroscopy. Appl. Nanosci. 12, 3399–3408. https://doi.org/10.1007/s13204-022-02550-2.

Leibetseder, F., Xie, J., Leeb, E., Hesser, G., Pettinger, K., Bretterbauer, K., 2024. Recyclable fluorine-free water-borne binders for high-energy lithium-ion battery cathodes. Adv. Energy Mater. 14. https://doi.org/10.1002/aenm.202401074.
Li, J., Le, D.B., Ferguson, P.P., Dahn, J.R., 2010. Lithium polyacrylate as a binder for tin-cobalt-carbon negative electrodes in lithium-ion batteries. Electrochim. Acta 55, 2991–2995. https://doi.org/10.1016/j.electacta.2010.01.011.
Li, M., Lu, J., Chen, Z., Amine, K., 2018. 30 years of lithium-ion batteries. Adv. Mater. 30. https://doi.org/10.1002/adma.201800561.
Li, S., Liu, Y.M., Zhang, Y.C., Song, Y., Wang, G.K., Liu, Y.X., Wu, Z.G., Zhong, B.H., Zhong, Y.J., Guo, X.D., 2021a. A review of rational design and investigation of binders applied in silicon-based anodes for lithium-ion batteries. J. Power Sources 485. https://doi.org/10.1016/j.jpowsour.2020.229331.
Li, Z., Wan, Z., Wu, G., Wu, Z., Zeng, X., Gan, L., Liu, J., Wu, S., Lin, Z., Gao, X., Ling, M., Liang, C., 2021b. A biopolymer network for lean binder in silicon nanoparticle anodes for lithium-ion batteries. Sustain. Mater. Technol. 30. https://doi.org/10.1016/j.susmat.2021.e00333.
Lim, S., Kim, S., Ahn, K.H., Lee, S.J., 2015. The effect of binders on the rheological properties and the microstructure formation of lithium-ion battery anode slurries. J. Power Sources 299, 221–230. https://doi.org/10.1016/j.jpowsour.2015.09.009.
Y. Liu, R. Zhang, J. Wang, Y. Wang, iScience perspective current and future lithium-ion battery manufacturing, (n.d.) https://doi.org/10.1016/j.isci.
Liu, Y., Liu, X., Zhu, Y., Wang, J., Ji, W., Liu, X., 2023. Scalable synthesis of pitch-coated nanoporous Si/Graphite composite anodes for lithium-ion batteries. Energy Fuels 37, 4624–4631. https://doi.org/10.1021/acs.energyfuels.2c03702.
Magasinski, A., Zdyrko, B., Kovalenko, I., Hertzberg, B., Burtovyy, R., Huebner, C.F., Fuller, T.F., Luzinov, I., Yushin, G., 2010. Toward efficient binders for Li-ion battery Si-based anodes: polyacrylic acid. ACS Appl. Mater. Interfaces 2, 3004–3010. https://doi.org/10.1021/am100871y.
Makino, S., Akimoto, Y., Ishii, M., Nakamura, H., 2024. Impact of slurry preparation method on the rheological behaviour of dense anode slurries for lithium-ion batteries. Rheol. Acta 63, 319–331. https://doi.org/10.1007/s00397-024-01440-4.
Mehigan, L., Ó Gallachóir, B., Deane, P., 2022. Batteries and interconnection: competing or complementary roles in the decarbonisation of the European power system? Renew. Energy 196, 1229–1240. https://doi.org/10.1016/j.renene.2022.07.058.
Montes, S., Beutl, A., Paolella, A., Jahn, M., Tron, A., 2024. Cost-effective solutions for lithium-ion battery manufacturing: comparative analysis of olefine and rubber-based alternative binders for high-energy Ni-rich NCM cathodes. Chemelectrochem 11. https://doi.org/10.1002/celc.202400465.
Mukanova, A., Nurpeissova, A., Kim, S.S., Myronov, M., Bakenov, Z., 2018. N-Type doped silicon thin film on a porous Cu current collector as the negative electrode for Li-Ion batteries. ChemistryOpen 7, 92–96. https://doi.org/10.1002/open.201700162.
Nguyen, B.P.N., Mariage, N., Fredon, R., Kelder, E.M., Lestriez, B., 2015. Manufacturing of LiNi 0.5 Mn 1.5 O 4 positive composite electrodes with industry-relevant surface capacities for Lithium Ion-cells. J. Electrochem. Soc. 162, A1451–A1459. https://doi.org/10.1149/2.0261508jes.
Obrovac, M.N., Christensen, L., 2004. Structural changes in silicon anodes during lithium insertion/extraction. Electrochem. Solid State Lett. 7. https://doi.org/10.1149/1.1652421.
Ouyang, L., Wu, Z., Wang, J., Qi, X., Li, Q., Wang, J., Lu, S., 2020. The effect of solid content on the rheological properties and microstructures of a Li-ion battery cathode slurry. RSC Adv. 10, 19360–19370. https://doi.org/10.1039/d0ra02651d.
Pieczonka, N.P.W., Borgel, V., Ziv, B., Leifer, N., Dargel, V., Aurbach, D., Kim, J.H., Liu, Z., Huang, X., Krachkovskiy, S.A., Goward, G.R., Halalay, I., Powell, B.R., Manthiram, A., 2015. Lithium polyacrylate (LiPAA) as an advanced binder and a passivating agent for high-voltage Li-Ion batteries. Adv. Energy Mater. 5. https://doi.org/10.1002/aenm.201501008.
Qin, T., Yang, H., Li, Q., Yu, X., Li, H., 2024. Design of functional binders for high-specific-energy lithium-ion batteries: from molecular structure to electrode properties. Indust. Chem. Mater. 2, 191–225. https://doi.org/10.1039/d3im00089c.
Ravesio, E., Montinaro, G., Mincuzzi, G., Negozio, M., Versaci, D., Gartiser, V., Lutey, A. H.A., Bella, F., Bodoardo, S., 2025. Ultrashort pulsed laser texturing of current collector for Si/C Li-ion anodes: characterization of electrochemical performance and evolution of interface morphology. J. Energy Storage 109. https://doi.org/10.1016/j.est.2024.115226.
Reynolds, C.D., Lam, J., Yang, L., Kendrick, E., 2022a. Extensional rheology of battery electrode slurries with water-based binders. Mater. Des. 222. https://doi.org/10.1016/j.matdes.2022.111104.
Reynolds, C.D., Hare, S.D., Slater, P.R., Simmons, M.J.H., Kendrick, E., 2022b. Rheology and structure of lithium-ion battery electrode slurries. Energy Technol. 10. https://doi.org/10.1002/ente.202200545.
Rolandi, A.C., de Meatza, I., Casado, N., Forsyth, M., Mecerreyes, D., Pozo-Gonzalo, C., 2024. Unlocking sustainable power: advances in aqueous processing and water-soluble binders for NMC cathodes in high-voltage Li-ion batteries. RSC Sustain. 2, 2125–2149. https://doi.org/10.1039/d4su00098f.
Román-Ramírez, L.A., Marco, J., 2022. Design of experiments applied to lithium-ion batteries: a literature review. Appl. Energy 320. https://doi.org/10.1016/j.apenergy.2022.119305.
T.W. Schwarz, G. Levy, H.H. Kawagoe, The Effect of pH on the Stability, n.d.
Scott, S., Islam, Z., Allen, J., Yingnakorn, T., Alflakian, A., Hathaway, J., Rastegarpanah, A., Harper, G.D.J., Kendrick, E., Anderson, P.A., Edge, J., Lander, L., Abbott, A.P., 2023. Designing lithium-ion batteries for recycle: the role of adhesives. Next Energy 1, 100023. https://doi.org/10.1016/j.nxener.2023.100023.
Sedlatschek, T., Frie, F., Weber, F., Sauer, D.U., Broeckmann, C., 2025. Continuous particle level operando observation of a composite graphite - SiO x electrode in a liquid electrolyte using scanning electron microscopy. J. Electrochem. Soc. 172, 090508. https://doi.org/10.1149/1945-7111/adfd3e.
Sharratt, W.N., Lopez, C.G., Sarkis, M., Tyagi, G., O'Connell, R., Rogers, S.E., Cabral, J.T., 2021. Ionotropic gelation fronts in sodium carboxymethyl cellulose for hydrogel particle formation. Gels 7, 44. https://doi.org/10.3390/gels7020044.
Sole, C., Drewett, N.E., Hardwick, L.J., 2014. Insitu Raman study of lithium-ion intercalation into microcrystalline graphite. Faraday Discuss 172, 223–237. https://doi.org/10.1039/c4fd00079j.
Song, J., Feng, Z., Wang, Y., Zhou, X., Zhang, X., Wang, K., Xie, J., 2019. Suppressed volume variation of optimized SiOx/C anodes with PAA-based binders for advanced lithium-ion pouch cells. Solid State Ionics 343. https://doi.org/10.1016/j.ssi.2019.115070.
Streipert, B., Stolz, L., Homann, G., Janßen, P., Cekic-Laskovic, I., Winter, M., Kasnatscheew, J., 2020. Conventional electrolyte and inactive electrode materials in lithium-ion batteries: determining cumulative impact of oxidative decomposition at high voltage. ChemSusChem 13, 5301–5307. https://doi.org/10.1002/cssc.202001530.
Sullivan, J.P., Bose, A., 2022. On the connection between slurry rheology and electrochemical performance of graphite anodes in Lithium-ion batteries. Electrochem. Commun. 141. https://doi.org/10.1016/j.elecom.2022.107353.
Sun, L., Su, T., Xu, L., Liu, M., Bin Du, H., 2016. Two-dimensional ultra-thin SiOx ($0 < x < 2$) nanosheets with long-term cycling stability as lithium ion battery anodes. Chem. Commun. 52, 4341–4344. https://doi.org/10.1039/c6cc00723f.
Sun, L., Liu, Y., Wu, J., Shao, R., Jiang, R., Tie, Z., Jin, Z., 2022. A review on recent advances for boosting initial coulombic efficiency of silicon anodic lithium ion batteries. Small 18. https://doi.org/10.1002/smll.202102894.
Tang, B., He, S., Deng, Y., Shan, Y., Qin, H., Noor, H., Hou, X., 2023. Advanced binder with ultralow-content for high performance silicon anode. J. Power Sources 556. https://doi.org/10.1016/j.jpowsour.2022.232237.
Truong, T.B.T., Chen, Y.R., Lin, G.Y., Lin, H.T., Wu, Y.S., Yang, C.C., 2021. Lithium polyacrylate polymer coating enhances the performance of graphite/silicon/carbon composite anodes. Electrochim. Acta 365. https://doi.org/10.1016/j.electacta.2020.137387.
Vanpeene, V., Huet, L., Villanova, J., Olbinado, M., Marone, F., Maire, E., Roué, L., Devic, T., Lestriez, B., 2025. Deciphering the benefits of coordinated binders in Si-Based anodes by combined Operando/In situ and Ex situ X-Ray Micro- and nano-tomographies. Adv. Energy Mater. 15. https://doi.org/10.1002/aenm.202403741.
Versaci, D., Apostu, O.D., Dessantis, D., Amici, J., Francia, C., Minella, M., Bodoardo, S., 2023. Tragacanth, an exudate gum as suitable aqueous binder for high voltage cathode material. Batteries 9. https://doi.org/10.3390/batteries9040199.
Xu, Y., Yin, G., Ma, Y., Zuo, P., Cheng, X., 2010. Nanosized core/shell silicon@carbon anode material for lithium ion batteries with polyvinylidene fluoride as carbon source. J. Mater. Chem. 20, 3216–3220. https://doi.org/10.1039/b921979j.
Yan, Z., Yi, S., Li, X., Jiang, J., Yang, D., Du, N., 2023. A scalable silicon/graphite anode with high silicon content for high-energy lithium-ion batteries. Mater. Today Energy 31. https://doi.org/10.1016/j.mtener.2022.101225.
Yang, L., Meng, T., Zheng, W., Zhong, J., Cheng, H., Tong, Y., Shu, D., 2024. Advanced binder design for high-performance silicon anodes. Energy Storage Mater. 72, 103766. https://doi.org/10.1016/J.ENSM.2024.103766.
Yi, W., Zhao, T., Li, D., Yuan, Q., Zhao, Z., Chen, B., Dang, N., 2025. Research progress of polyacrylate binders for Silicon-based anodes in lithium-ion batteries. Chem. Eur J. 31. https://doi.org/10.1002/chem.202500321.
Yin, S., Ji, Q., Zuo, X., Xie, S., Fang, K., Xia, Y., Li, J., Qiu, B., Wang, M., Ban, J., Wang, X., Zhang, Y., Xiao, Y., Zheng, L., Liang, S., Liu, Z., Wang, C., Cheng, Y.J., 2018. Silicon lithium-ion battery anode with enhanced performance: multiple effects of silver nanoparticles. J. Mater. Sci. Technol. 34, 1902–1911. https://doi.org/10.1016/j.jmst.2018.02.004.
Yuca, N., Kalafat, I., Guney, E., Cetin, B., Taskin, O.S., 2022. Self-healing systems in silicon anodes for Li-Ion batteries. Materials 15. https://doi.org/10.3390/ma15072392.
Zhang, L., Deng, J., Liu, L., Si, W., Oswald, S., Xi, L., Kundu, M., Ma, G., Gemming, T., Baunack, S., Ding, F., Yan, C., Schmidt, O.G., 2014. Hierarchically designed SiOx/SiOy bilayer nanomembranes as stable anodes for lithium ion batteries. Adv. Mater. 26, 4527–4532. https://doi.org/10.1002/adma.201401194.
Zhang, X., Ge, X., Shen, Z., Ma, H., Wang, J., Wang, S., Liu, L., Liu, B., Liu, L., Zhao, Y., 2021. Green water-based binders for $LiFePO_4$/C cathodes in Li-ion batteries: a comparative study. New J. Chem. 45, 9846–9855. https://doi.org/10.1039/D1NJ01208H.
Zhang, Y.T., Xue, J.X., Wang, R., Jia, S.X., Zhou, J.J., Li, L., 2024. Cross-linkable binder for composite silicon-graphite anodes in lithium-ion batteries. Giant 19. https://doi.org/10.1016/j.giant.2024.100319.
Zhao, X., Yim, C.-H., Du, N., Abu-Lebdeh, Y., 2018. Crosslinked chitosan networks as binders for Silicon/Graphite composite electrodes in Li-Ion batteries. J. Electrochem. Soc. 165, A1110–A1121. https://doi.org/10.1149/2.114805jes.
Zhao, B., Yin, D., Gao, Y., Ren, J., 2022. Concentration dependence of yield stress, thixotropy, and viscoelasticity rheological behavior of lithium-ion battery slurry. Ceram. Int. 48, 19073–19080. https://doi.org/10.1016/j.ceramint.2022.03.197.
Zhong, L., Sun, Y., Shen, K., Li, F., Liu, H., Sun, L., Xie, D., 2024. Poly(Acrylic Acid)-Based polymer binders for high-performance lithium-ion batteries: from structure to properties. Small 20. https://doi.org/10.1002/smll.202407297.